NOVA SCHOOL OF SCIENCE & TECHNOLOGY

DEPARTAMENT OF PHYSICS

MARGARIDA MENDES GONÇALVES CORDEIRO PIRES

BSc in Engineering Physics

PHYSICS OF EUV SOURCE: IMPACT OF EUV PLASMA GENERATION ON THERMO-MECHANICS OF CO_2 LASER SOURCE

MASTER IN ENGINEERING PHYSICS

NOVA University Lisbon

September, 2023

DEPARTAMENT OF PHYSICS

PHYSICS OF EUV SOURCE: IMPACT OF EUV PLASMA GENERATION ON THERMO-MECHANICS OF CO_2 LASER SOURCE

MARGARIDA MENDES GONÇALVES CORDEIRO PIRES

BSc in Engineering Physics

Co-advisers: Daniel Martins
PhD in Engineering Physics, ASML

Maria Isabel Simões Catarino
Assistant Professor, NOVA University Lisbon

MASTER IN ENGINEERING PHYSICS

NOVA University Lisbon
September, 2023

Physics of EUV source: Impact of EUV plasma generation on thermo-mechanics of CO_2 laser source

This document was created with Microsoft Word text processor and the NOVAthesis Word template [37].

ACKNOWLEDGEMENTS

Completing Physics Engineering has been a challenging yet immensely rewarding journey, and I would like to take this opportunity to express my gratitude to those who have been instrumental in its successful completion.

First and foremost, I would like to express my deepest appreciation to my co-advisors Daniel Martins and Prof. Isabel Catarino for their unwavering support, guidance, and mentorship throughout this process. Their expertise, dedication, and insightful feedback have significantly shaped the direction and quality of this research, with which I learn a lot from.

I'm extremely grateful for ASML, as well as for creating a high-quality work environment that I had the privilege of being a part of. This experience has not only enriched my professional journey but also allowed me to contribute to meaningful work, which could not have been undertaken without the guidance and dedication of my Team Leader, Bart Petri. I also want to thank Andrey Tychkov, Deniz Mutlu, Jonghoon Jang and Stijn Moonen, whose knowledge, feedback and contributions were nothing short of invaluable, and this project's success would not have been possible without their dedication.

My family deserves a special mention for encouraging me to step away from my comfort zone and leave my country for this experience. Their belief in my abilities and their willingness to stand by me during this journey meant the world to me. I am deeply thankful for their love, guidance, and the sacrifices they made to help me seize this opportunity for personal and professional growth.

To my boyfriend Tomás, there are simply no words to describe his support, patience, time, understanding, encouragement, and belief in me. Thank you for being my rock every single day, and this entire experience would unquestionably not be the same without you, even if you were more than 1800 kilometers away.

To my friends Rúben, Catarina, Joana and Tiago for the conversations and shared moments when I longed for the feeling of home. Your friendship, understanding and comfort made this challenging journey much more enjoyable. I am profoundly grateful for your friendship and the sense of belonging you have bestowed upon me.

And finally, a sincere thank you to everyone who I had the opportunity to share my experience in Eindhoven, whether they were colleagues at ASML or people I met in the city. Ultimately, it was the connections I forged and the invaluable lessons I learned from everyone that made this entire journey truly worthwhile.

"In any moment of decision, the best thing you can do is the right thing. The worst thing you can do is nothing." – Theodore Roosevelt.

ABSTRACT

Extreme Ultraviolet (EUV) lithography is a cutting-edge technology that plays a pivotal role in semiconductor manufacturing, which has enabled the production of smaller and more powerful electronic components. Efforts to continuously boost EUV power translate to higher throughput, allowing more wafers to be processed. This, in turn, decreases production costs and enhances the overall productivity of semiconductor fabrication.

However, the trend of elevating EUV power, raises preoccupation over the thermo-mechanical stability of optical components that constitute these lithography machines. Because they operate with high precision systems, small uncontrolled disturbances can produce losses of performance, which is the case with the thermo-mechanical impact of back-reflected heat loads in the Focusing Optics (FO). This is the module that includes the optical components and structures that interacts with both the high-power CO_2 drive laser (forward beam), used to generate EUV, and the back-reflected heat loads from the EUV generation (return beam and EUV back-reflections).

The primary goal of this research was to investigate how the increase in EUV power generation impacts a population of multiple machines. This investigation employed a MATLAB script to quantify back-reflected heat loads in the FO module. The analysis highlighted that 3 components within this module are particularly susceptible. Notably, the structure responsible for compensating for CO_2 laser focus shifts, with an actuation system, provided insights into the link between back-reflected power and the systems' correction, which implies a wider actuator range of motion. It was found the bigger contributor for CO_2 laser focus shift, within the FO components. This insight holds significance in preventing reaching an actuation limit, due to the generation of higher-power back-reflections.

Keywords: Extreme Ultraviolet Lithography (EUV), Thermo-Mechanical Stability, Back-Reflected Heat Loads, Semiconductor Fabrication

RESUMO

A litografia por *Extreme Ultraviolet* (EUV) é uma tecnologia de vanguarda que desempenha um papel fundamental na fabricação de *microchips*, permitindo a produção de componentes cada vez mais pequenos e potentes. Os esforços para aumentar continuamente a potência do EUV resultam numa maior taxa de produção, possibilitando o processamento de mais *wafers*. Isto, por sua vez, resulta numa redução de custos de produção e num melhoramento da produtividade na fabricação de *microchips*.

No entanto, a tendência para aumentar a potência do EUV suscita preocupações quanto à estabilidade termo-mecânica dos componentes óticos que constituem estas máquinas de litografia. Uma vez que operam com sistemas de alta precisão, pequenas perturbações não controladas podem levar a perdas de performance, como é o caso do impacto termo-mecânico das cargas térmicas refletidas de volta para o *Focusing Optics* (FO). Este módulo engloba as estruturas e componentes óticos que interagem, tanto com o laser de CO_2 de alta potência, usado para gerar EUV, como com as cargas térmicas geradas pela produção de EUV, que incluem o próprio EUV e parte do laser de CO_2 que é refletido de volta para o FO.

O principal objetivo desta tese foi investigar o impacto da produção de maiores potências de EUV, com uma população de diversas máquinas. Esta investigação recorreu à programação de um *script* de MATLAB para quantificar as cargas térmicas nas estruturas do FO. A análise destacou os três componentes do FO que são particularmente afetados. Por outro lado, o sistema de atuação, responsável por compensar os desvios do foco do laser de CO_2, proporcionou uma compreensão aprofundada sobre a estrutura cuja expansão térmica mais contribui para tal desvio, e provoca uma amplitude cada vez maior do movimento do atuador. Este resultado é significativo para melhor se compreender como prevenir atingir-se um limite de atuação, devido ao aumento da potência das cargas térmicas no FO.

Palavras-chave: Litografia de Extreme Ultraviolet (EUV), Estabilidade Termo-Mecânica, Cargas Térmicas Refletidas, Produção de Semicondutores

CONTENTS

LIST OF FIGURES

LIST OF TABLES

ACRONYMS

ACT	Actuator
BTS	Beam Transport System
CE	Conversion Efficiency
DL	Drive Laser
DUV	Deep Ultra-violet
EUV	Extreme Ultra-violet
FB	Forward beam
FO	Focusing Optics
IF	Intermediate Focus
LPP	Laser-Produced Plasma
MOPA	Master Oscillator Power Amplifier
MP	Main Pulse
PP	Pre-Pulse

1

INTRODUCTION

1.1 Motivation

EUV photolithography is currently the most advanced technology for microchip manufacture, due to its ability to print the smallest wafer patterns the world has seen [1]. The size of these machines speaks for itself when it comes to complexity, where the EUV generation stage alone requires extreme amounts of precision for the whole lithography process to function [2]. To produce EUV, it is required a CO_2 drive laser to hit a tin droplet, which generates the EUV plasma [3], a process that is later explained. The high power of these two light sources impacts the thermo-mechanics of the structures that interact with them [4], the expansion of which may bring consequences for the performance and lifespan of EUV lithography machines.

The trend continues to be the generation of higher EUV power, which is why the thermo-mechanical impact of high-power sources must be investigated. The Focusing Optics (FO) module, which includes the optical components the focus the high-power CO_2 drive laser on the tin droplet [3], is the module that receives more heat loads. The thermal expansion of any structure, if not properly controlled, can contribute to a loss of performance or even catastrophic consequences. For this reason, this project tries to answer to the questions:

- What is the overall impact of the heat loads in the FO?
- What structures in the FO are mostly impacted by back-reflected heat loads?
- How does increasing back-reflected power impact the system that compensates for expansions in the FO (the actuator)?
- What is the structure in the FO, the expansion of which is mostly contributing for the actuator's compensation?

1.2 Project goals

Before beginning the deep dive into this research, it is also important to understand the goals of this project and how the questions previously stated are answered. Because this is research that took place at the EUV lithography machines' manufacturer, ASML, the main goal is to provide the company with knowledge regarding the impact of the heat loads in the Focusing Optics, and the thermal and thermo-mechanical performance of several EUV machines, contributing for a better product in the future.

This is accomplished through the access and processing of machine data, with the development of a MATLAB script, which is the focus of the chapter 3, *Methodology*. Following the data processing steps, statistical data of a population of several EUV machines is achieved, which ultimately reveals the magnitude of the heat loads in the FO. Finally, the final goal is to study of the impact of heat loads the system that compensates for expansions in the FO (the actuator), conceiving a mathematical method that helps understanding the consequences of higher EUV power generation in the actuation range.

1.3 Location of the research

This research took place at ASML's headquarters, in Veldhoven, the Netherlands. ASML is the single manufacturer of EUV lithography machines and one of the main manufacturers of deep ultra-violet (DUV) lithography machines. This project was possible thanks to the ASML's financing and support, and to the opportunity of monetary aid from the Erasmus+ scholarship.

1.4 Thesis outline

This thesis is organized in 5 chapters: Introduction, Literature review, Methodology, Results and Conclusions. In chapter 1, is described the motivation and goals of the project, while in chapter 2, a brief description of the state-of-the-art technology of EUV generation and the contextualization of this research in the future of EUV lithography. It is also described the physical concepts utilized throughout this thesis. In chapter 3, the methods followed to create the MATLAB script are explained, from the importing of raw machine data to data appropriate for analysis and statistics. In chapter 4, it is analyzed the results obtained from chapter 3's methods and draws conclusions regarding the impact of back-reflected heat loads in the FO, obtaining the answers to the questions from the motivation section, 1.1. Finally, chapter 5 summarizes the key conclusions of the research, and it is delineated the future work proposed in order to continue this study.

2

LITERATURE REVIEW

2.1 Background and current trends in photolithography

In a constantly advancing technological world, our daily lives are becoming easier day after day. Computers are faster, smartphones have progressively more features, and so many other unimaginable tools of our everyday life are helping us become more and more comfortable. But the key to all these advancements is the progress made by the chip-making industry. Although Moore's Law may be coming to an end, it is still relevant for explaining the speed at which the world is advancing with better and faster technology.

Photolithography is a cornerstone technology in the manufacture of microelectronics and is used in the production of a wide range of integrated circuits, memory devices, and microprocessors [5]. DUV (193nm) lithography is the current main technology for chip-printing [6], but the most powerful and advanced technology in use today is the EUV photolithography, with a wavelength of 13.5nm, which can print the smallest microchips available so far, reaching a logic node size of 3nm [7].

Over the last 40 years, the light source has seen its wavelength reduced, with the goal of decreasing the node size [8]. Mercury arc lamps were used to produce visible g-line light (436nm), used in the first wafer stepper [9]. Then ultraviolet i-line (365nm) light was proposed, reaching a 0.7µm resolution [10]. After that, DUV began its way, using KrF excimer lasers as the light source, with a wavelength of 248nm [11]. Advancements on DUV lithography allowed the wavelength of the light source to be reduced even more, with the use of an ArF excimer laser for 193nm DUV (dry and immersion) [12].

Currently, the three market leaders in the chip-making industry are ASML, Nikon, and Canon DUV. The competition remains on DUV market, with ASML being the leader on immersion systems, shown in Figure 2.1, and the leader on ArF, KrF and i-line systems, since 2016, as shown in Figure 2.2. The EUV market, though, is fully controlled by ASML, which until today was the only company selling EUV systems [13].

Figure 2.1: Number of immersion systems sold by ASML and Nikon by fiscal year. Source: [6]

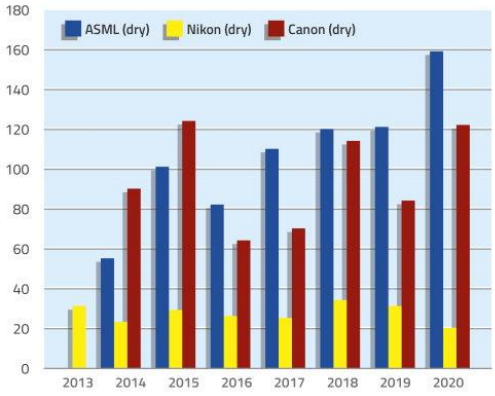

Figure 2.2: Number of ArF, KrF and i-line systems sold by ASML, Canon and Nikon by fiscal year. Source: [6]

2.2 EUV lithography

Unlike the previous technology, which uses a laser as the light source, EUV is instead generated using a technique called Laser-Produced Plasma (LPP) [14], which consists of the formation of a plasma when a drive laser is focused on a target. In the case of EUV, the drive laser is a high-power CO_2 laser system, and the target is a tin droplet of about 25µm [15]. Figure 2.3 shows the system that generates and amplifies the CO_2 drive laser, the Beam Transport System (BTS), and the FO, which focuses the DL on the tin droplet.

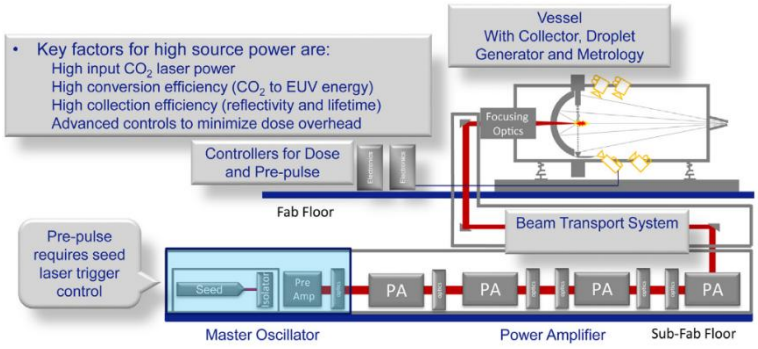

Figure 2.3: Schematics of the modules that constitute the EUV source, from the seed laser to the generation of plasma, focused on the IF. Source: [16]

Tin is the material of choice due to its high EUV conversion efficiency (CE) [2], which is one of the most important requirements for producing EUV light more efficiently. CE is the ratio of an energy output over the amount of energy that was put into producing it. In this case, the higher the CE of a target, the more EUV power, at 13.5nm, it can provide.

The system involved in generating the tin plasma is a very powerful CO_2 laser, that achieves more than 20kW [17]. It includes a master oscillator power amplifier (MOPA), which generates a laser pulse that seeds the power amplifiers for single pass gain, shown in Figure 2.4 [18]. This way, a seed laser can be amplified, and its power scaled. This process is more beneficial than just using a higher-power laser since lower-power seed lasers provide a lower noise amplitude and increased pulse-to-pulse stability [19]. Current machines also use a

high-power seed system technology [18], because of the need to scale the drive laser power even more.

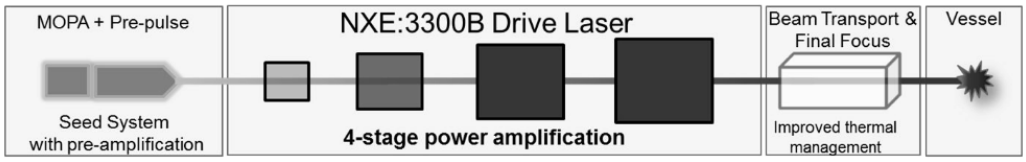

Figure 2.4: Schematics of the MOPA+PP system. Source: [19]

Another important component present is a pre-pulse (PP) system, whose function is to re-shape the tin droplet [21]. It was found that a cloud-like shape could provide a higher CE, as shown in Figure 2.5. Therefore, before the main laser is focused on the tin droplet, it is hit by a primary laser that generates an expanded cloud target. Figure 2.6 demonstrates the principle behind it, where it is shown that the CE increases with the cloud-like target shapes. But even with this approach, the CE achieved is only 5% [17]. Despite the inefficiency of EUV generation, the TWINSCAN NXE:3600D, shown in Figure 2.7, and the TWINSCAN NXE:3400C are the current EUV machines on the market, capable of achieving the current most advanced microchips.

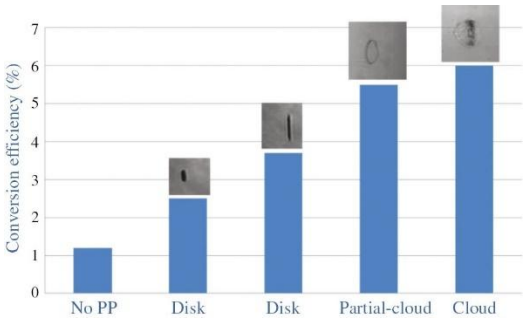

Figure 2.5: Conversion efficiency with various target shapes and densities. Source: [20]

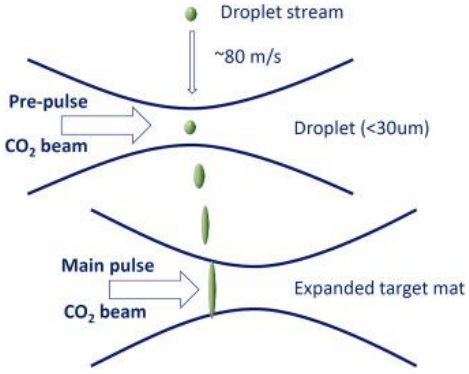

Figure 2.6: Target formation process and principle. Source: [16]

The big obstacle with EUV light is its high absorption by any material [22], which comes with a lot of power loss from all the system constituents. Several measures were taken to have into account this property of EUV light. Firstly, the system is in a vacuum because air particles also absorb [23]. And secondly, the focusing optics use mirrors instead of lenses since they would also absorb all the EUV light.

Another difficulty is the fact that the plasma formed emits not only EUV radiation but also a much broader spectrum of light. So, it's important that the mirrors can select only the 13.5nm wavelength to deliver the EUV beam with the correct wavelength to the to the intermediate focus (IF). The collector mirror, the mirror responsible for that function, is designed to provide an overall peak reflectivity at the 13.5nm wavelength [24]. However, in theory, the maximum reflectivity of this approach is still 75% [25]. The collector also has an ellipsoidal shape, as can be observed in Figure 2.8, because this is the shape that allows light to be reflected and converge on the IF.

Figure 2.7: TWINSCAN NXE: 3600D. Adapted from: [26]

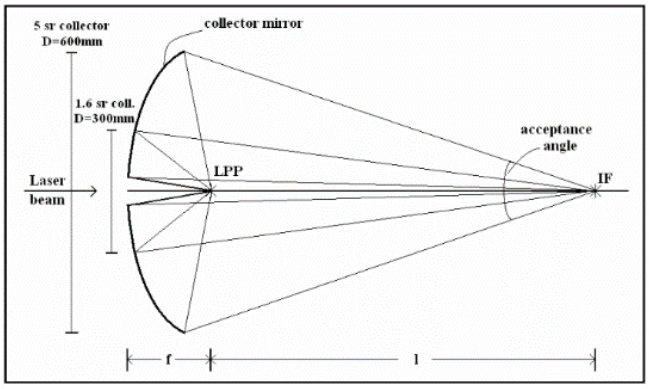

Figure 2.8: Light collection configuration with ellipsoidal mirror for refocusing the EUV radiation from the LPP to the IF. Source: [27]

Power loss is still observed throughout the whole system. To get an idea of the power loss level, it was concluded that for a throughput of 100 silicon wafers per hour (WPH) at a typical scanner duty cycle of 60%, the power at the wafer should be greater than about 550mW, which requires the EUV source power at IF to be greater than 200W [20]. But even though large amounts of power are needed to fabricate chips with EUV technology, they are still the only machines capable of doing so.

2.2.1 The Focusing Optics

The FO is the module in research. As previously mentioned, the proximity of this module from the vessel, as represented in Figure 2.9, leaves the components inside on the FO exposed to back reflected light from the vessel, which causes them to thermally expand.

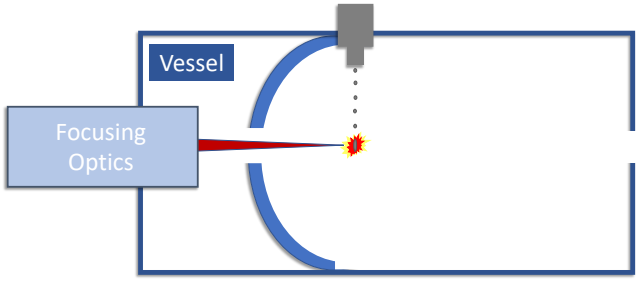

Figure 2.9: Representation of the FO and the Vessel in the process of generating EUV.

To study the impact of the heat loads in the FO, it's important to know what structures are inside of it and what role they play. In Figure 2.10, it is observed the order of which the CO_2 drive laser interacts with each structure. There are two optical components, OC1 and OC2, and three mirrors, M1, M2 and M3. These five structures directly interact with the CO_2 drive laser beam, either by transmitting it or reflecting it. There are also two other structures, that although don't have an optical function, are still exposed from heat loads from the vessel, which are the Housing, which is a structure in which the components are attached to or built on, and the ACT (Actuator), which is responsible for moving the M3 mirror, to keep the laser focused on the droplet.

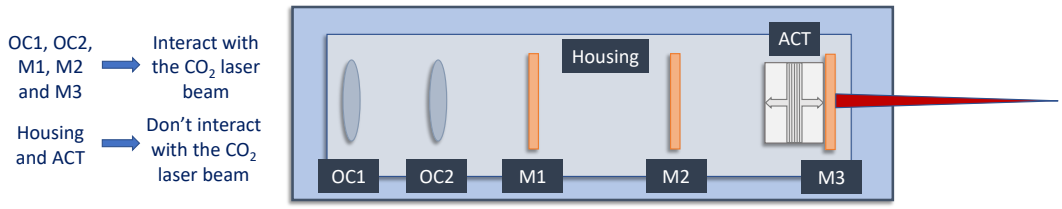

Figure 2.10: Schematic of the order of the structures inside the FO (Not a real representation of their position)

So, the main takeaway of this section is to understand the components that are studied in this project. Because these components interact with high power radiation, they are water-cooled, to keep their temperature stable and avoid large thermal expansion. The temperature of the water carries the information about heat loads and their impact, so it's important to know how the cooling water systems work and how water temperature can be measured.

2.2.2 Water-cooling systems

All structures in the FO have their own water-cooling system, to keep them at a controlled temperature, despite the high heat loads from the CO_2 drive laser beam. Heat loads are measured through changes in the cooling water temperature, since it can give us information about the power absorbed in the component. A particularity about these systems is that the water-cooling system for the optical components is separated from the remaining structures, which can be observed in Figure 2.11 and Figure 2.12. Another particularity is that only the outlet water temperature is accessible, which requires aid from the MATLAB script, to obtain the variation in temperature, ΔT, in each component. Finally, M1 and M2 have a joint water-cooling system, which isn't be an obstacle in any way, only something to remember when analyzing data.

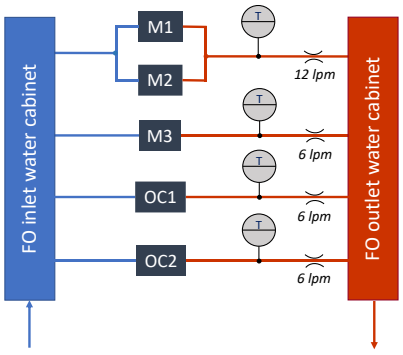

Figure 2.11: Cooling water system for optical structures

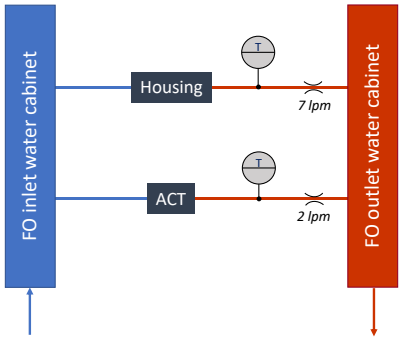

Figure 2.12: Cooling water system for the Housing and ACT

2.2.3 The actuator

The purpose of the ACT is to control the focus position of the CO_2 drive laser and maximize the generation of EUV power. To do this, the ACT can move up and down to keep the drive laser focused on the tin droplets, as it is seen in Figure 2.13. This is achieved with control modules that send a feedback signal of the droplet's position in relation to the actuator, so

that it can follow the instruction to move accordingly. The interesting fact about the ACT is that the thermal expansion in the FO causes shifts in the drive laser focus position, that must be corrected with the ACT. This means that this structure can provide information about the impact that the FO expansion, or back-reflections, have in the actuator's range.

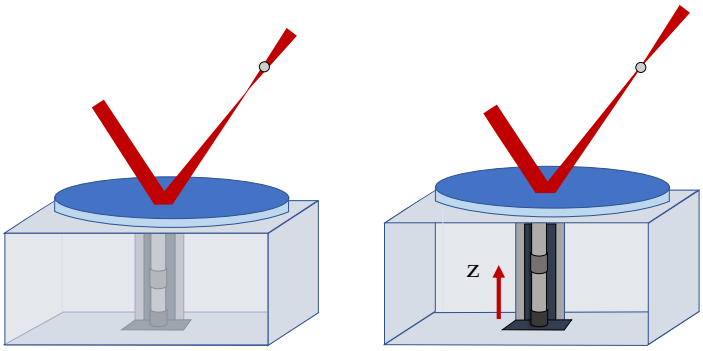

Figure 2.13: Actuator's motion to keep the CO_2 laser focus on the droplet.

2.3 EUV and CO_2 drive laser

2.3.1 Absorption from materials

It is important to distinguish the difference between the materials' interaction with EUV light and CO_2 laser light. In the first one, we're dealing with 13.5nm radiation, but the second one has a wavelength of about 10.6µm. This difference of about three orders of magnitude highly affects the way light is absorbed and reflected. In Figure 2.14, it is observed that for the CO_2 laser wavelength, the absorption in the material depicted is low. On the other hand, when the wavelength becomes shorter, the absorption increases, sometimes exponentially. Therefore, for the EUV wavelength, the absorption is very high, not just for metals but for most intermediums [25].

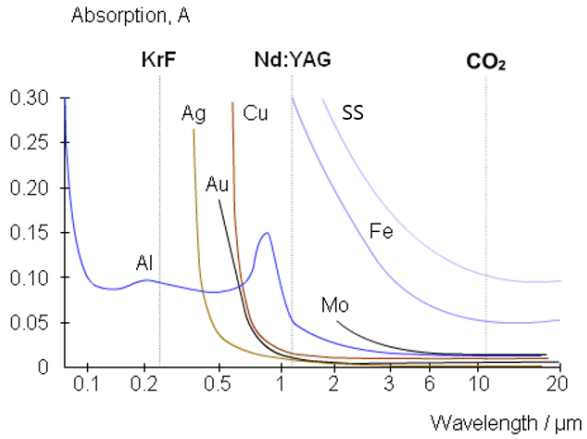

Figure 2.14: Absorption coefficient for several materials. Adapted from: [28].

2.3.2 Back-reflections

Back-reflections occur because of the vessel's architecture where both EUV and CO_2 laser can be back-reflected.

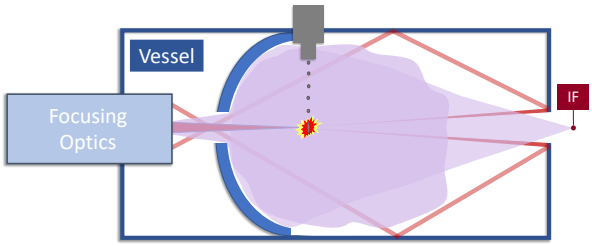

Figure 2.15: Back-reflections

2.4 Heat transfer and thermal properties

This chapter discusses the theoretical ideas that must be understood to fully comprehend the guiding principles that underlie the objectives of this project. Among these concepts, are the main ways heat can be transferred within the FO components.

2.4.1 Thermal conduction and thermal expansion

Thermal conduction consists of the transfer of heat through molecular interaction and displacement [29]. It persists until the material achieves thermal equilibrium. The speed at which the heat is transferred depends on the temperature difference and the material's thermal conductivity. The heat flux obtained by conduction is expressed in the equation 1, where k is the thermal conductivity (W/m·K), A is the surface area (m^2) and $\Delta T/\Delta x$ is the temperature gradient (K/m).

$$\dot{q}_k = kA\frac{\Delta T}{\Delta x} \tag{1}$$

The thermal conductivity of the instruments is a very important property to consider. When a material has a high thermal conductivity, it can distribute heat more uniformly and efficiently, preventing temperature gradients and its deformation. Together with a high thermal conductivity, it is also essential that the material has a low thermal expansion coefficient, so that it is less susceptible to deformation from temperature variations. This is key to maintaining a mechanically stable system. Figure 2.16 shows various materials classified by their thermal conductivity and thermal expansion. It's easy to conclude that the materials that better suit a system with high heat loads would be those at the bottom right, with high thermal conductivity and low thermal expansion, namely the metals.

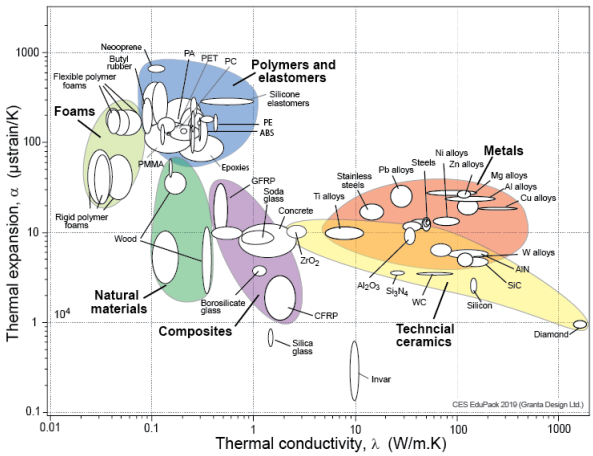

Figure 2.16: Thermal expansion vs. thermal conductivity for various materials. Source: [30].

2.4.2 Thermal time constant

Time constant, τ, is a parameter that measures the time it takes for a system to change, given a stepwise variation of the initial conditions [31].

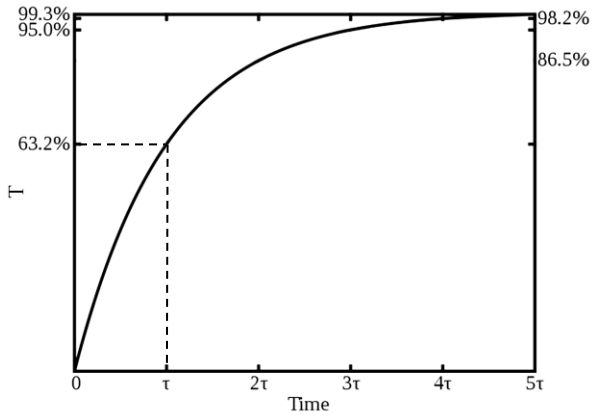

Figure 2.17: Temperature curve during heating

In a thermodynamic system, τ measures the time it takes for a system to reach 63.2% of the new surrounding temperature from the initial temperature (in the case of a positive temperature variation), in an exponential rising, as seen in Figure 2.17. This way, if there is a sudden increase in temperature, it varies according to the equation 2:

$$T(t) = (T_0 - T_\infty)e^{-\frac{t}{\tau}} + T_\infty \tag{2}$$

With:

$$\tau = RC \tag{3}$$

Where R is thermal resistance and C is the heat capacity.

2.4.3 Heat capacity

Heat capacity quantifies the amount of heat energy a material can store for each unit change in temperature [32]. The heat transfer can be defined as the equation 4, where c is the specific heat capacity (J/kg·K), m is the mass of the material (kg), and ΔT is the variation in temperature of the material (K).

$$Q = cm\Delta T \tag{4}$$

This property is especially useful to calculate the absorbed power by the water-cooling systems. This can be done as shown in equation 4, so the power that is being absorbed, $\dot{Q}$ depends on the mass flow, m/t (kg/s), on the specific heat capacity of water, $c_{p,water}$ (J/kg·K), and on the temperature variation, ΔT, of the water (K).

In Table 2.1, there can be found the thermal coefficients mentioned of a few metals used in EUV lithography machines [33]–[35]. Comparing with Figure 2.16 these are some of the materials at the bottom-right of the chart, which mean that their low thermal expansion and high thermal conductivity is appropriate for the thermomechanical stability of the machine's optics.

Table 2.1: Thermal properties of Al, Cu, SS and Ti [33]–[35]

Metal	Thermal conductivity, k (W/m·K)	Specific heat, c_p (kJ/kg·K)	Thermal expansion, α (10^{-6} m/m°C)
Al	236	0.91	23.1
Cu	401	0.39	16.8
SS	14.4	0.5	17.8
Ti	22.4	0.54	8.5 - 9

2.4.4 Convection and radiation

As mentioned, the environment for the EUV production is a vacuum, so heat transfer through gas conduction or convection is negligible. Thermal radiation is defined as the electromagnetic energy emitted when a body is at a nonzero temperature [36]. The thermal radiation power transferred between two bodies is given by the equation 5, where T_1 and T_2 are the temperatures of surfaces 1 and 2, σ is the value of the Stefan Boltzmann constant, 5.670367 × 10^{-8} W/m² and ϵ is the emissivity of surface 1.

$$\dot{q}_{rad} = \varepsilon\sigma A(T_1^4 - T_2^4) \tag{5}$$

In this case, radiation has a negligible impact in the FO structures cooling, due to the similar temperatures between structures and FO environment.

3

METHODOLOGY

As previously mentioned, MATLAB was the software chosen for the creation of a tool that allowed this research to take place. Thus, the *Methodology* chapter focuses on every step of the MATLAB tool creation and follows the path between the raw signals that are provided by sensors inside the machine, in their working conditions, and the statistics and plotting of all machines' data. The reason why the MATLAB tool creation deserves its own chapter is because, to reach the statistical analysis step, a significant amount of machine data processing was done beforewards.

3.1 Creating a tool in MATLAB

In Figure 3.1, it is shown all the steps that need to be fulfilled for the tool creation, that is discussed in this chapter:

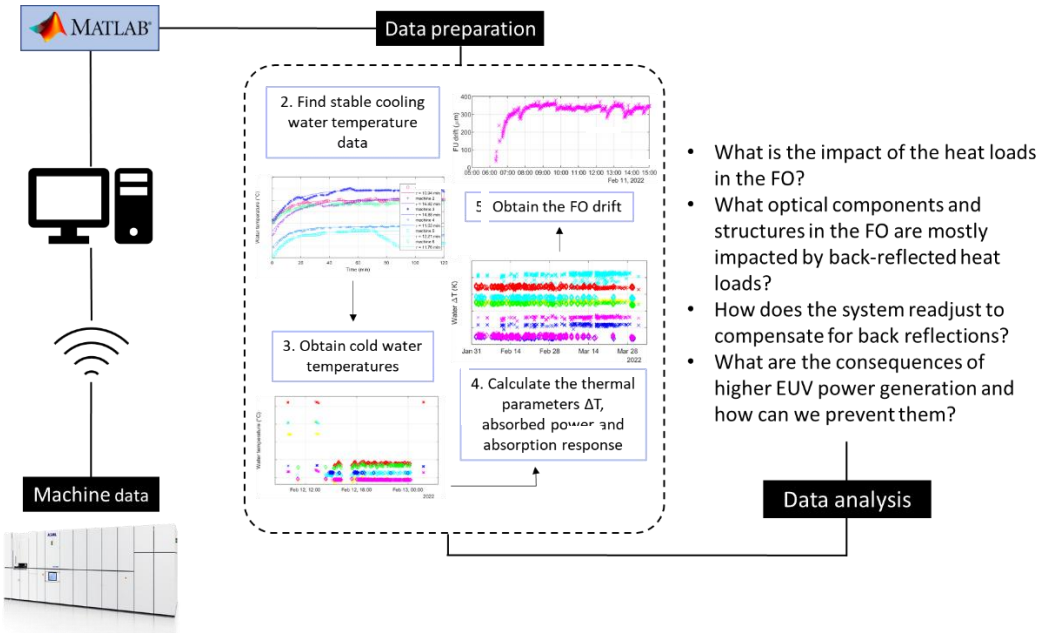

Figure 3.1: Schematic of the MATLAB tool data preparation.

3.2 Data collection

Data collection is done through a direct connection between MATLAB and the machine's databases. This part of the script was provided to allow the import of machine's data for this study, which is raw minutely data from sensor signals.

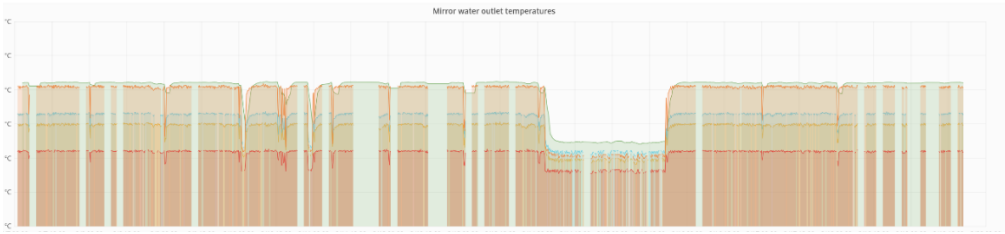

Figure 3.2: Example of raw temperature data from mirrors.

3.3 Heat loads in the Focusing Optics

In this section, the goal is to obtain the thermal parameters, water's ΔT, absorbed power and absorption response, of each FO structure's cooling water, to collect statistical data to ultimately understand the magnitude and impact of back-reflections on the FO. Figure 3.3 shows an example of the temperature signal the cooling water of each FO structure, where temperatures can very between 21°C and 23°C.

However, not all thermal data is useful for statistics. At around 11:00, in Figure 3.3, when the CO_2 drive laser is switched ON, the cooling water does not stabilize immediately. Therefore, it should be waited until the water's temperature has stabilized to count as useful data for statistics.

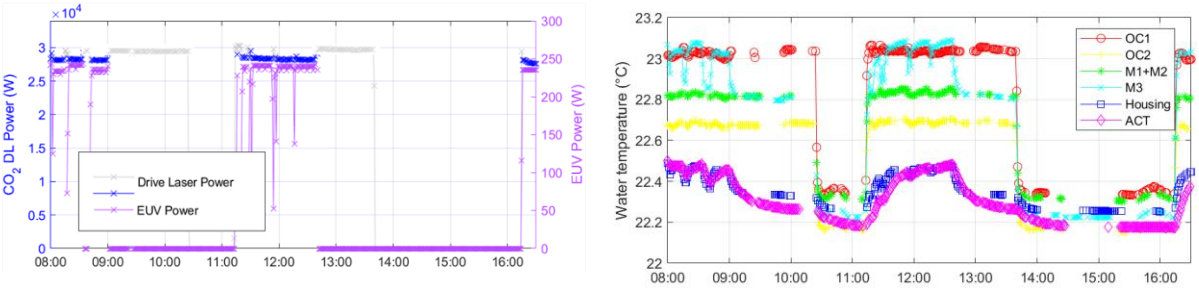

Figure 3.3: EUV power and CO2 drive laser power (left) and raw temperatures from FO (right).

3.3.1 Obtaining stable water temperatures

Analyzing the water temperature, In the right graph of Figure 3.3, the housing's water and the ACT's water are the ones that require more time to stabilize. Moreover, for the sake of simplifying the MATLAB tool, rather than assigning individual stabilization times to each structure, the approach of adopting the slowest stabilization time for all FO structures is employed. Therefore, it is sufficient to examine the water in the housing and the water in the ACT to identify the slowest stabilization time.

To find the slowest stabilization time, 6 different machines were picked to calculate the exponential time constant of the housing and ACT. It was used the *Curve Fitter* in MATLAB, to fit the water temperature data, when the drive laser is switched ON, to an exponential curve. Having different machines is important for the accuracy of the results, because the EUV variation affects the temperature data, causing lower quality fittings. Figure 3.4 shows the 6 obtained fittings, for both the housing and ACT water, and their respective time constant, while table 1 gathers the average of each structure's water time constant.

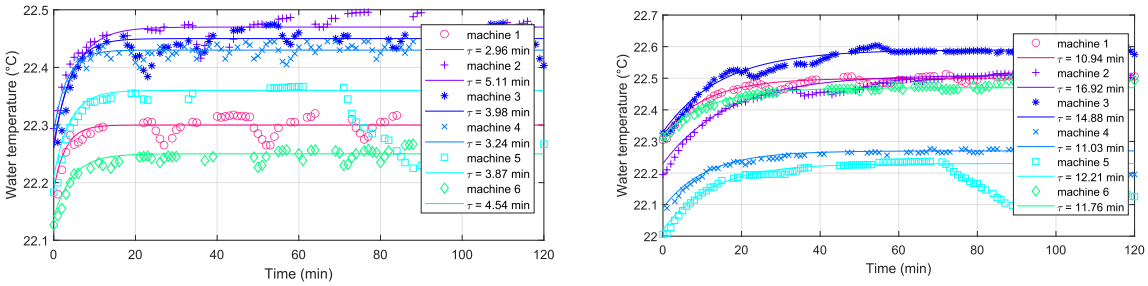

Figure 3.4: Housing water (left) and ACT water (right) temperature variation and correspondent exponential fittings for 6 machines.

Table 3.1: Time constants for the housing and ACT water and respective average and standard deviation, for 6 machines.

	Time constant (min)	
Machine	Housing water	ACT water
1	2.96	10.94
2	5.11	16.92
3	3.92	14.88
4	3.24	11.03
5	3.87	12.21
6	4.54	11.76
Avg., μ	3.9	13
St. Dev., σ	0.73	2.2

From Table 3.1, the ACT has the slowest stabilizing cooling water, therefore the stabilization of the entire FO takes place with the stabilization of this structure's water. As shown in Figure 2.17, a 95% stabilization corresponds to a time of 3τ, equating to approximately 40 minutes of stabilization time.

However, it is important to consider that this is the timeframe one should wait before initiating data collection if the system's state remains unchanged. Put differently, when the system has just been turned ON, the countdown of 40 minutes begins.

Row	CO_2 Total Laser Power (W)	EUV Power (W)	
1	0	0	
2	24367.508	206.051	Machine ON: start counting 40 minutes
3	24290.900	234.051	
(...)	(...)	(...)	
21	23319.424	164.546	(count interrupted before 40 minutes)
22	24311.656	176.653	
23	24325.616	238.845	Machine ON: start counting 40 minutes
(...)	(...)	(...)	
62	24240.953	204.534	
63	24289.607	243.753	(machine ON for 40 minutes: **stable data**!)
64	24239.424	234.846	

Figure 3.5: Representation of the MATLAB script for obtaining stable data.

In Figure 3.5, it is demonstrated the idea behind the MATLAB tool, to implement a stabilization time. In this case, 1 if the machine has been ON for 40 minutes or more, the data is considered stable. Any interruption sets the clock back to zero. Figure 3.6 showcases the CO_2 drive laser power in stable states, in blue, and non-stable in grey.

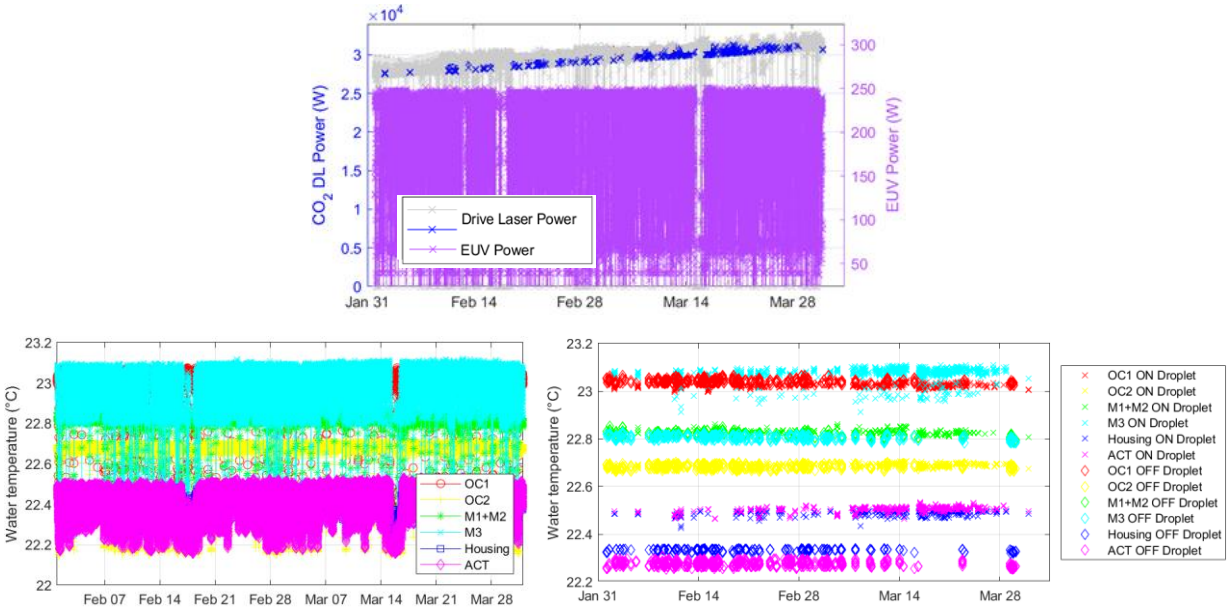

Figure 3.6: Drive laser power (top), raw water temperatures (bottom left) and stable water temperatures, with a 30-minute stabilization time (bottom right).

In the example shown in Figure 3.6, it was not possible to find data that satisfied the 40-minute stabilization time. Therefore, the stabilization time had to be reduced to 30 minutes, affecting the accuracy of the obtained data. However, this is something that must be compromised to collect enough data for statistical analysis.

3.3.2 Calculating the thermal parameters under study

The next step is to calculate the thermal parameters that are analyzed in this project: water's ΔT, absorbed power, and absorption response. This comparison provides insights into the impact of back-reflections within the FO. These parameters are determined using the stable temperature values just obtained:

$$\Delta T = T_{hot} - T_{cold} \tag{6}$$

$$\text{Abs. Pwr} = \frac{Q_{abs}}{t} = \frac{m\, c_{p,water}\, \Delta T}{t} \tag{7}$$

$$\text{Abs. Resp.} = \frac{\Delta T}{FB_{CO_2\,DL}\; power} \tag{8}$$

The absorption response is a parameter that measures the temperature variation per unit of power of the CO_2 forward beam absorbed. Recalling the details about the water-cooling systems in section 2.2.2, T_{cold} values are not available. Consequently, an alternative approach must be devised to acquire cold temperature data. This alternative is necessary for calculating the water's ΔT and other parameters that hinge on this information.

3.3.2.1 Obtaining cold water temperatures

Examining Figure 3.7, which illustrates distinct CO_2 drive laser states, it's evident that a corresponding decrease in water temperature occurs when the drive laser is turned OFF. If the drive laser is not operating, then there are no heat sources interacting with the FO, which allows its structures, and consequently their cooling water, to cool down The water temperature eventually reaches a temperature that is the same of the inlet cooling water, T_{cold}. This temperature decrease also requires some time to stabilize, which is the reverse process of finding the stable T_{hot}. The difference lies in the fact that the time constant now denotes the duration required for the temperature to decrease from its initial value to 36.8% of the newly established ambient temperature. Analogously, a 40-minute stabilization interval can be implemented to gather cold water temperatures. Figure 3.7, on the right, provides a representation of the stable hot and cold temperatures.

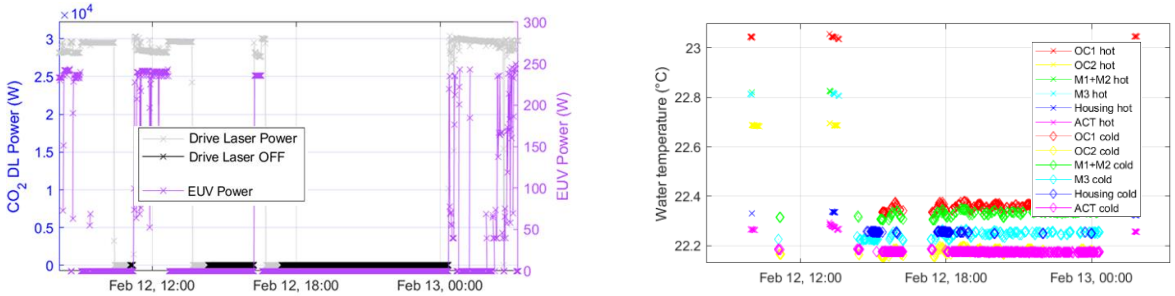

Figure 3.7: CO_2 drive laser indicating the stable laser OFF state, in black (left), and cold-water temperatures (right), with a 40-minute stabilization time for cold water.

To calculate the ΔT, it requires a simple calculation using the obtained stable hot and cold-water temperatures. To do this, the ΔT is calculated subtracting the average of immediately preceding cold water values to each T_{hot} value. The plot in Figure 3.8 demonstrates how it is done: for the cold temperatures at the larger rectangle, it is calculated each average; with this

average the ΔT is calculated for the hot temperatures after 00:00 of February 13th. The next time water temperature gets cold, the same process is repeated.

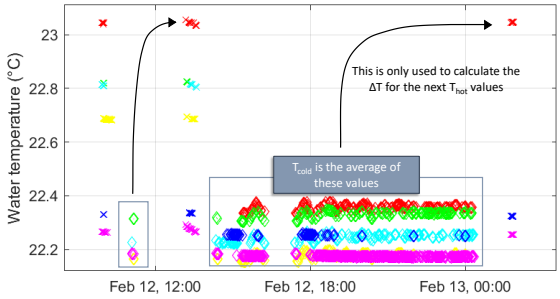

Figure 3.8: Idea behind the calculation of the cold temperature and ΔT.

Figure 3.9 shows the three calculated parameters, for the machine in study: the temperature variation, the absorbed power, and the absorption response.

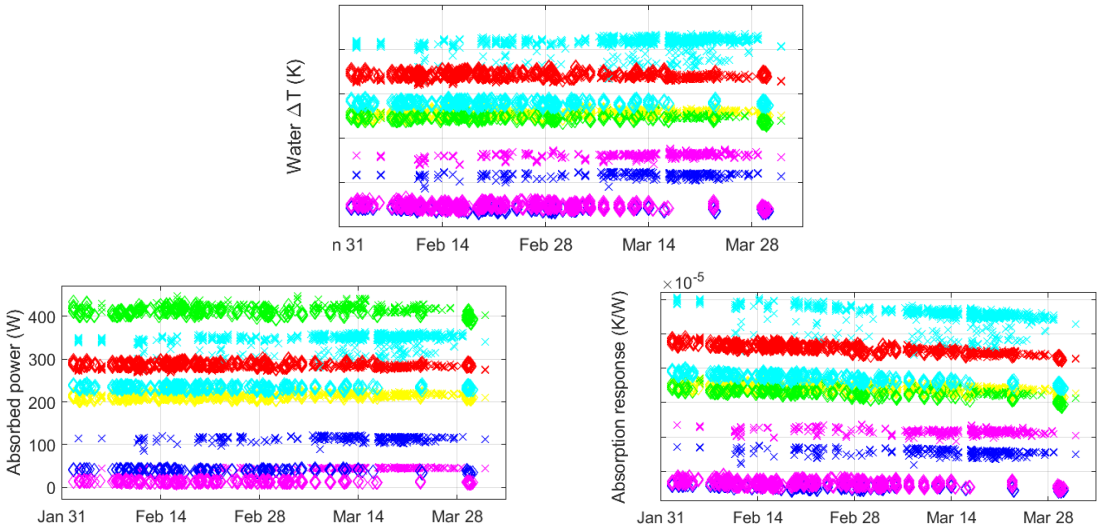

Figure 3.9: Thermal parameters calculated for 1 machine, with a 30-minute stabilization.

3.4 The actuation range

The ACT moves in the perpendicular (Z) direction to keep the drive laser focused on the droplet. When the DL is switched ON, for at least a few seconds, no EUV is being generated to allow the optical components to heat up. This heating process results in thermal expansion of the mirrors that quicky overshoots the DL focus, which requires the Actuator to compensate. Figure 3.10, shows this phenomenon, where there is an apparent difference in compensation between two machines: machine A appears to require a bigger actuation in the -Z direction than machine B.

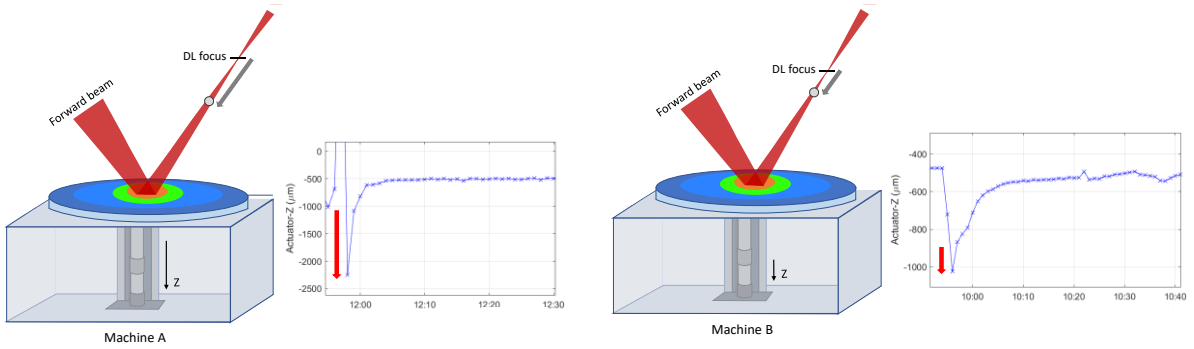

Figure 3.10: Example of two machines' Actuator-Z signals, where machine A (left) shows a bigger compensation than machine B (right).

However, the full picture may not be seen, as the data is gathered minutely, but this compensation occurs very quickly, which may be hiding intermediate data. For example, in machine B, a lower Actuator-Z position may not be visible. Therefore, to understand the relationship between back-reflected power and the correction by the Actuator, to study the impact of increasing back-reflections, simply using the Actuator movement signal is not enough. However, it is possible to indirectly get a signal that informs about the focus correction itself.

In short, there are two signals that collectively illustrate the ACT compensation:

- **Actuator-Z,** which is the ACT movement in Z; ACT position.
- **Droplet relative to Actuator**, which shows the droplet's position relative to the Actuator-Z position. For every Actuator-Z position there is a correspondent Droplet relative to Actuator position. In reality, the droplet does not change position.

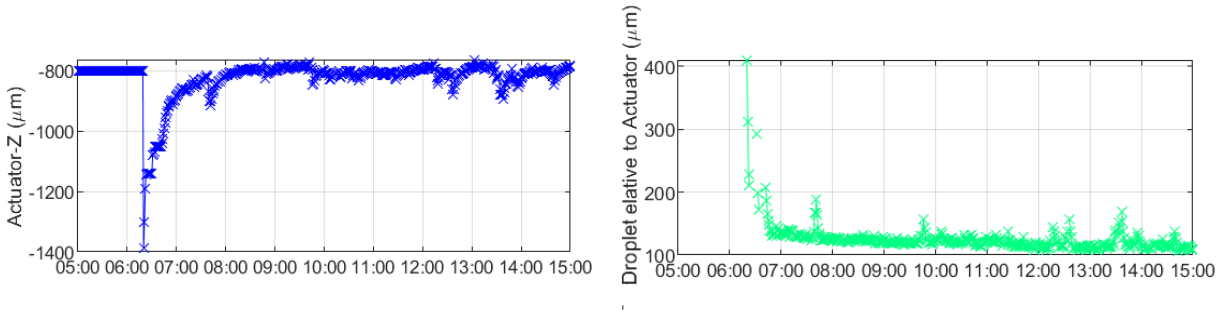

Figure 3.11: Example of Actuator-Z and Droplet relative to Actuator signals

The Droplet relative to Actuator signal is only available when there is a detected droplet. For this reason, the issue with not detecting the real Actuator-Z minimum doesn't exist if these two signals are summed, because this quick adjustment occurs when structures are still heating up and no EUV is being generated (no Droplet relative to Actuator signal available). This sum results in a signal that is a measurement of the focus drift's correction, after the DL focus overshoot correction, as if the point of view would be looking at the droplet from the FO, in the DL direction.

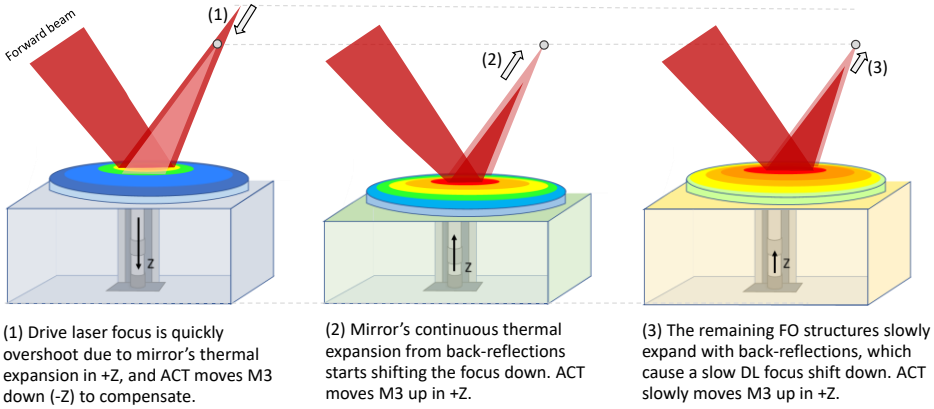

Figure 3.12: Description of the different stages of the actuation process.

Figure 3.12 helps understanding the stages of the ACT correction of the focus drift. As mentioned, the focus drift correction starts at the end of stage (1), because this compensation happens quickly. What happens next is a focus drift due to continuous thermal expansion, from back-reflections, which causes the DL beam to get more divergent, shifting its focus down. The third image represents the impact of the slower expanding structures (higher time constant), which cause a less drastic focus drift.

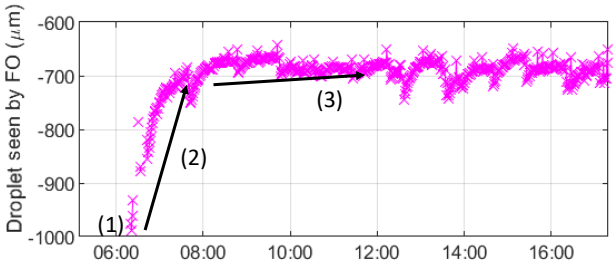

Figure 3.13: Example of the Droplet seen by FO signal, where it is seen the correspondent stages from Figure 3.12.

Figure 3.13 shows the obtained Droplet seen by FO signal, which ultimately informs about the focus drift from the ACT correction of the FO thermal expansions.

3.4.1 Obtaining the FO drift

Dealing with absolute positions is impractical due to variations between machines. Therefore, it is best to offset it to 0 the Droplet seen by FO signal, to obtain the focus drift from the FO expansions' compensation, a signal named FO drift.

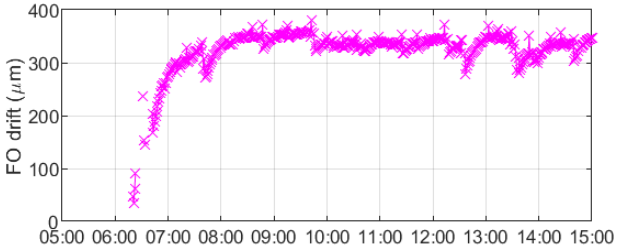

Figure 3.14: Example of the FO drift signal

This drift is expected to grow with higher back-reflected power, which is related to a bigger ACT compensation. As EUV power tends to increase, it's crucial to avoid exhausting the actuation range. The next chapter provides statistical results to understand the impact of back-

reflections on the FO and find the root cause of the substantial FO drift. This insight guides efforts to prevent reaching the maximum ACT range.

3.5 Visualizing machine data

The next chapter focuses on the statistical results obtained with the data processed with the MATLAB tool. This data is mostly shown in violin plots. These plots show the probability density of the data at different values, smoothed by a kernel density estimator.

As seen in Figure 3.15, they are extremely helpful to visualize differences between data from the structures' cooling water, with a violin plot for each component's cooling water, in 1 machine. These plots are read by measuring numeric values of a certain parameter in the vertical axis, and the respective frequency of occurrence for each in the horizontal axis. The dots help visualizing the median of each plot, which also have two horizontal grey lines, that represent the first and third quartile.

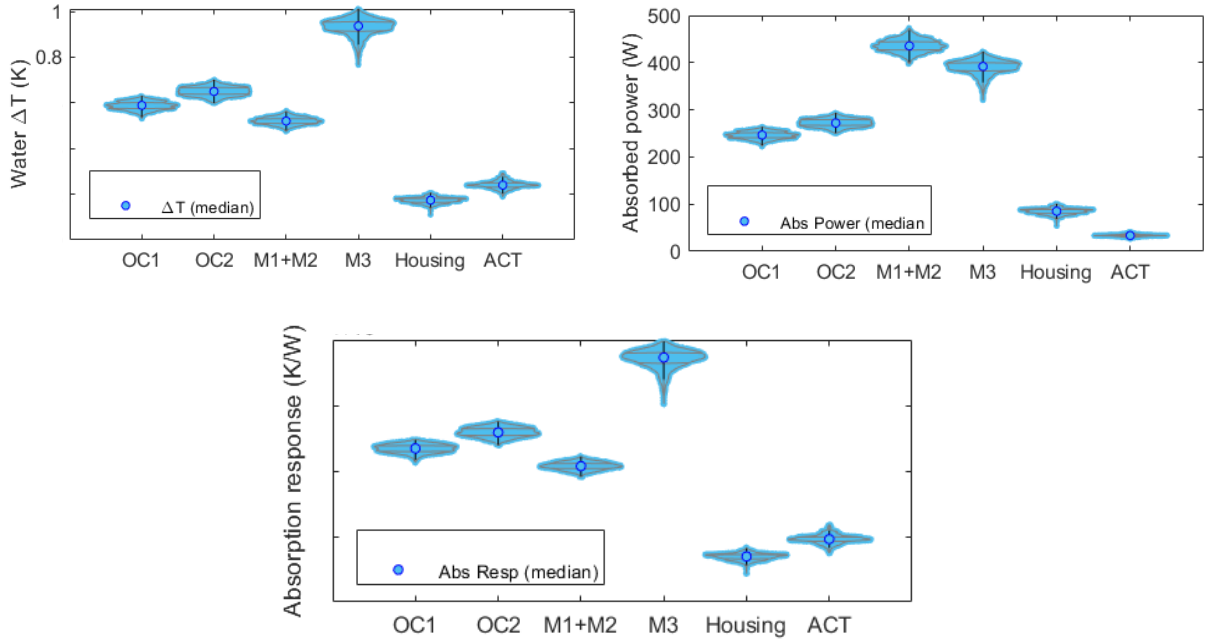

Figure 3.15: Violin plots for thermal data statistics for 1 machine

From this machine, some observations can already be stated:

- The M3 shows the highest temperature variation (the absorbed power from M1+M2 is higher because it includes the water flow from these two mirrors summed).
- The biggest absorption response is seen for M3, which means that possibly this structure is getting more impacted by back reflections, which must be confirmed with a population of more machines.
- Finally, absorption response data from Housing and ACT, suggest that these two structures are also getting impacted by back-reflections, otherwise it would be zero (they don't reflect the drive laser's forward beam).

3.5.1 Calculating expected machine data in MATLAB

Optical components, that reflect the drive laser beam are designed to achieve a maximum reflectivity of its wavelength, minimizing the absorbed CO_2 laser heat loads at the same time. Because their reflectivity values are specified by manufacturing, the expected absorbed laser power, from the forward beam, can be calculated. However, instead of having a distribution of expected absorbed power values, due to the distribution in drive laser power, the median for the expected absorbed power can be obtained.

$$Abs.FB\ Pwr_{(median)} = median\left(FB_{CO_2\ DL}\ power\ \times\ reflectivity\right) \tag{9}$$

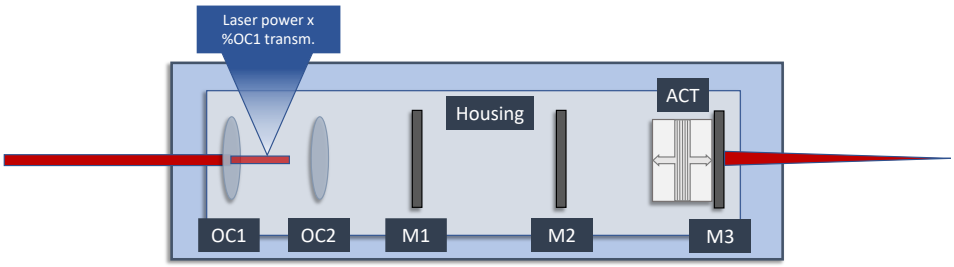

Figure 3.16: Schematic of the CO_2 drive laser power loss after interacting with OC1.

To obtain the theoretical value of the forward beam absorption by the FO components, it must be considered the successive absorptions by each structure that reflects/transmits the forward beam. Following Figure 3.16, the forward beam, after being transmitted by OC1, has less power when it interacts with OC2, since a small percentage of the radiation is absorbed by OC1. In addition, OC1 itself is also not receiving the entire CO_2 drive laser power that is achieved in the power amplifiers, due to the absorption from the beam transport system's optical components.

$$Abs.FB\ Pwr_{OC1\ (median)} = median\left(FB_{CO_2\ DL}\ power\ \times\ BTS_{transm.} \times (1 - OC1_{transm.})\right) \tag{10}$$

$$Abs.FB\ Pwr_{OC2\ (median)} = median\left(FB_{CO_2\ DL}\ power\ \times\ BTS_{transm.} \times OC1_{transm.} \times (1 - OC2_{transm.})\right) \tag{11}$$

However, as it is seen in Figure 3.17, some errors are exacerbated, when only one machine is being analyzed, which is the case of the OC1 depicted. Here, the theoretical absorption is higher than the plotted data, which practically would not make sense: what is absorbed by the structures can only be equal or higher than the absorbed power from the forward beam, because of additional absorption from back-reflected radiation.

Assuming design values, for the water flow reflection/transmission coefficients, for example, can be among the plotting errors, since degradation or slight manufacturing imperfections result in a diversion from the actual forward beam absorption. Assuming an approximate and fixed value for the BTS absorption, when the BTS can change from machine to machine, can also impact the result.

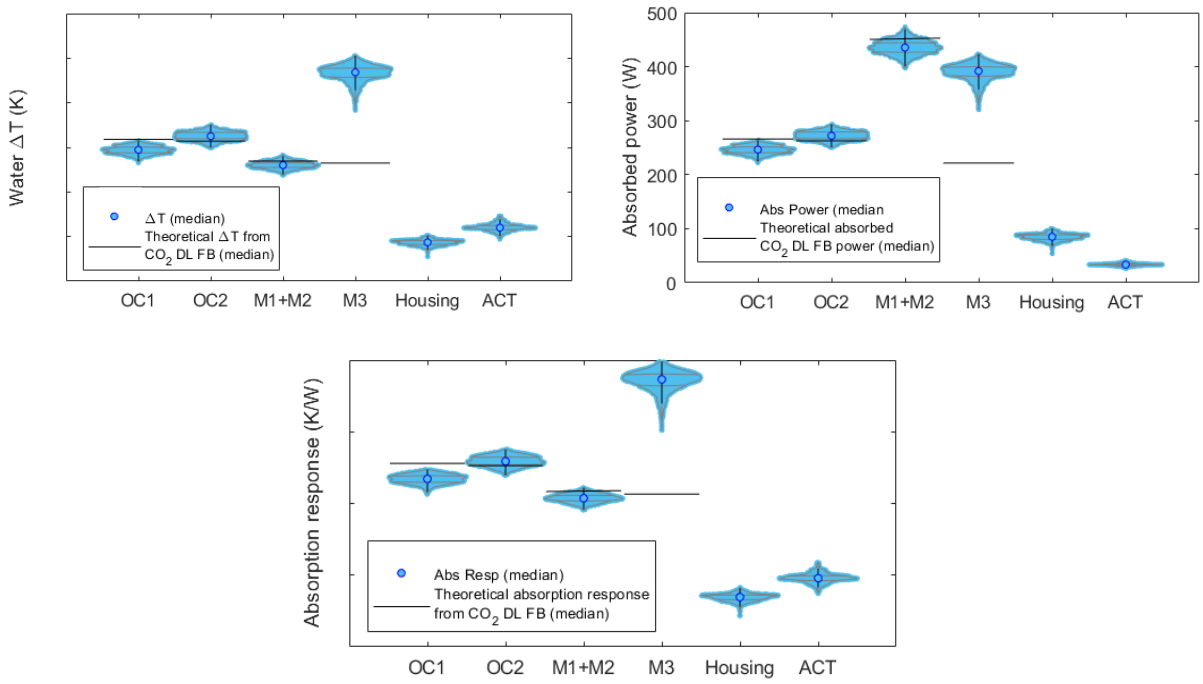

Figure 3.17: Violin plots for thermal data statistics for 1 machine and the theoretical FB effect on the ΔT, its absorbed power, and the theoretical FB absorption response

Nevertheless, the large difference between the theoretical FB absorption response of the M3 and the measured data, suggests that this mirror is also impacted by back-reflected heat loads.

4

RESULTS

4.1 MATLAB tool overview

This chapter focuses on the statistical results obtained with the data processed with the MATLAB tool, where the workflow is described in detail and a summary is depicted in Figure 4.1.

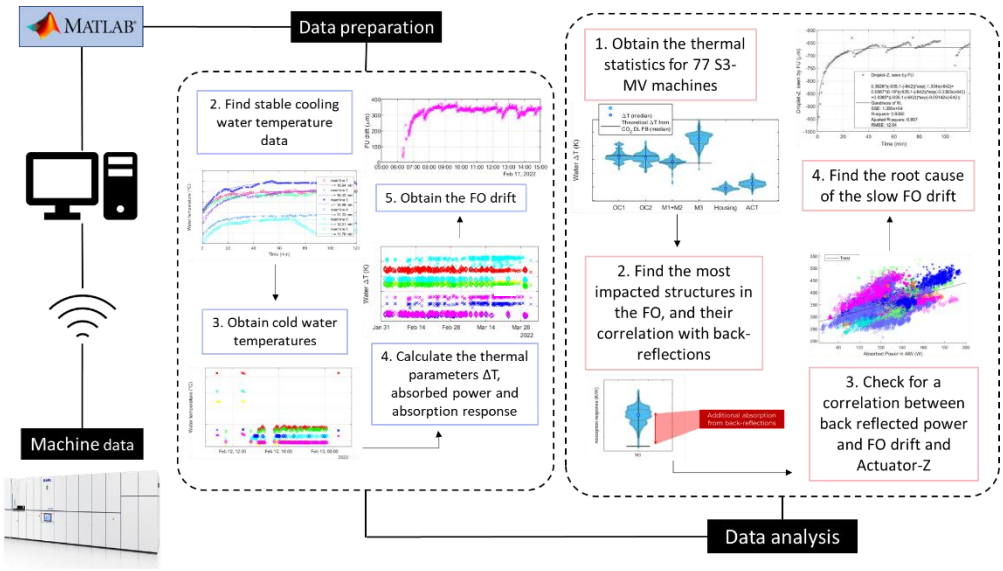

Figure 4.1: MATLAB tool overview with the data analysis steps.

4.2 Thermal data statistics for all machines

Figure 3.17 showed that the absorbed power by M3 has some dispersion. Its exposure to back-reflections, also means that the more power is being generated, the more power is absorbed. For one machine, these effects might not be obvious, but for a population of machines, results get more disperse due to machines operating at varying EUV and DL power.

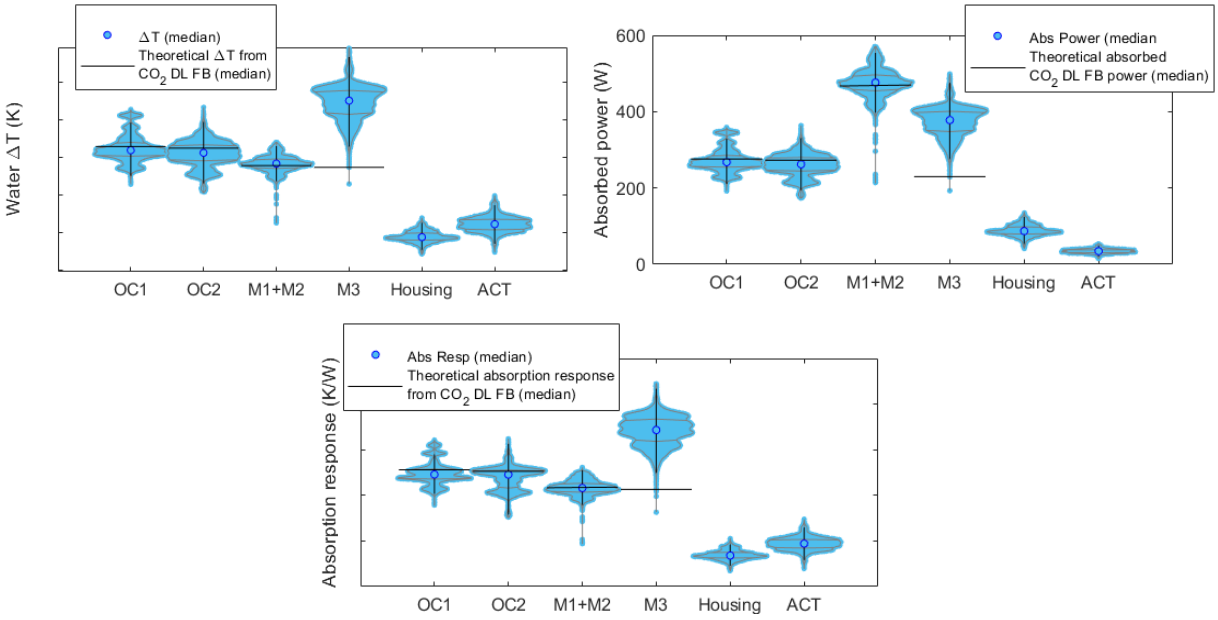

Figure 4.2: Violin plots of the thermal parameters for a population of several machines, including the median of the theoretical values.

As it is seen in Figure 4.2, with population of multiple machines, it's concluded that the three most impacted structures by back-reflected heat loads, in the FO, are indeed the M3, the Housing and the ACT, where the evidence of this impact detailed in Figure 4.3. The remaining optics do not show an influence from back-reflected heat loads in their thermal data.

Figure 4.3: Explanation of the back-reflections impact evidence

4.3 Correlation between back reflected power and absorbed power

Given that back reflections impact the M3, the Housing and the ACT, it is predictable that the more drive laser power, the more power is absorbed. Therefore, it's also important to understand, not only what structures are impacted by back-reflections, but also how much they are impacted.

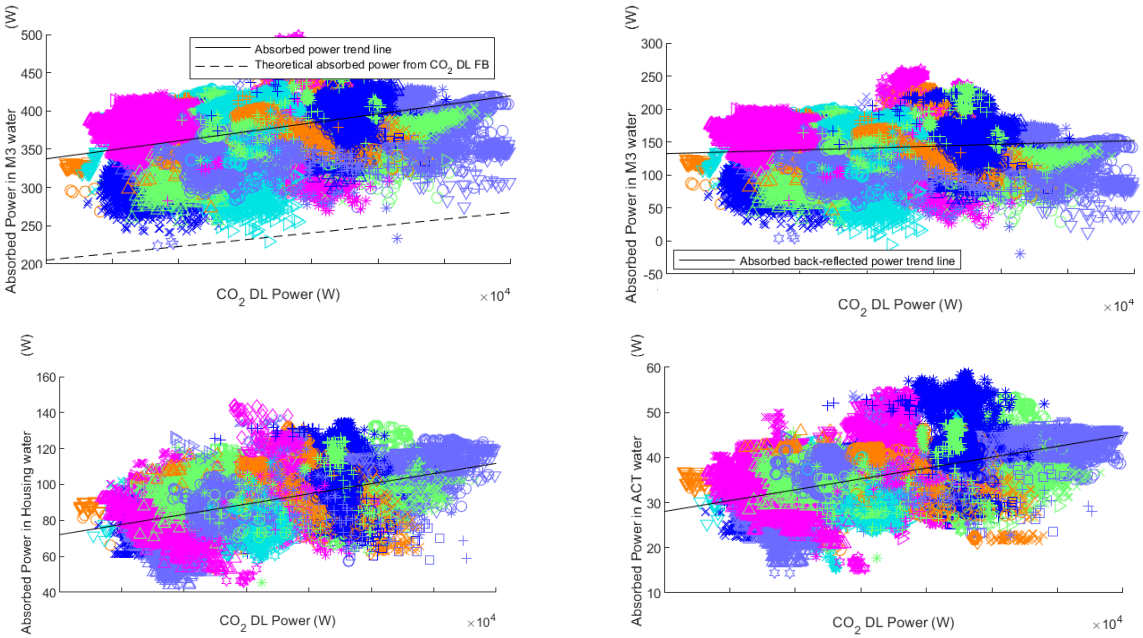

Figure 4.4: Correlation between DL power and absorbed power on M3 (top left), absorbed back-reflected power on M3 (top right), absorbed power in Housing (bottom left) and ACT (bottom right) (each color and shape is a different machine)

Figure 4.4 shows the obtained plots, where the one for M3 also includes the theoretical absorption of the forward beam line. In the top-right plot, it is seen that a large portion of the absorbed power by the M3 is coming from back-reflections and correlates with the increasing CO_2 laser power. But, if for every machine it is subtracted the theoretical forward beam absorption, the correlation seems to disappear, at the top-left plot. Two things may be causing this:

- EUV absorption may be prevailing over CO_2 back-reflected laser absorption, which is expected because M3 has a high reflectivity for the drive laser's wavelength but highly absorbs the EUV wavelength, and there is no correlation between EUV and CO_2 drive laser power.
- The theoretical forward beam value assuming fixed BTS absorption values and optics' coating absorption coefficients values, that vary from machine to machine. For this reason, when the absorbed power for every machine is subtracted by the theoretical forward beam absorption, the result can get very different from the expectation.

4.4 Impact of back reflections in the actuation range

As previously mentioned, the study of the ACT is important, to understand what happens when there is an increasing back-reflected heat loads. When it comes to increasing FO thermal expansions, which shift the laser focus and need to be compensated by the Actuator, increasing back-reflections raise the concern regarding the exhaustion of the actuation range, from continuous focus drift.

4.4.1 Correlation between back-reflected power and actuation range

With the stable statistical data, it is possible to correlate it with the back reflected power. However, the exact back reflected power is not known, but the power absorbed in Housing/ACT water is a measurement of back-reflections, since these structures don't reflect the forward beam. In Figure 4.5, the FO drift and Actuator-Z range are plotted with the back-reflected power. The Actuator-Z range values are obtained by simply offsetting the minimum Actuator-Z value to 0, for every machine.

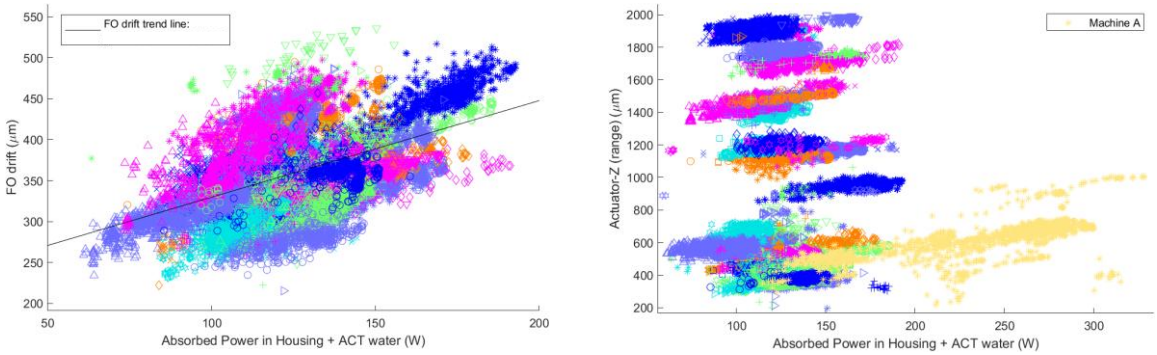

Figure 4.5: Correlation between FO drift and absorbed power in Housing+ACT water (left) and between Actuator-Z range and absorbed power in Housing+ACT water (right) (each shape and color represent one machine).

The correlation between the FO drift and the absorbed back-reflection is clear, which means that the focus is expected to continuously drift from the FO thermal expansions. This FO drift is directly related to the Actuator-Z range, which even though it is a signal that is not practical for this research, as explained in section 3.5, still shows individual correlations with increasing back-reflections, corroborate with Machine A, which is a different machine with higher back-reflection levels. Thus, higher back-reflections will implicate a higher actuation range.

4.5 Contributors to the FO drift

The study of the thermo-mechanical stability of the FO is now focused on the impact that the FO structure' thermal expansion has on the actuation range, more specifically, which structure is possibly contributing the most for the actuator's correction. As it is known, the structures in the FO do not expand uniformly because they are impacted differently by back-reflections and have different water-cooling systems that increase their stabilization. Knowing the biggest contributor helps in the intervention in case of large actuation ranges or in preventing an actuation range limit.

4.5.1 FO drift and raw temperatures

The similarity between the FO drift and the FO structures' cooling water raw temperatures, shown in Figure 4.6, demonstrates that the focus is drifting and being corrected by the ACT, according to the structures' expansions (raw temperature increase). Given the fact that the optics stabilize quickly, and the Housing and ACT require a longer period to stabilize, the FO drift appears in two stages:

- Fast drift: The optics quickly absorbs the heat loads; both optical and non-optical structures are expanding.
- Slow drift: Optical components have stabilized, while Housing and ACT keep increasing its temperature which contributes for the slower part of the FO drift.

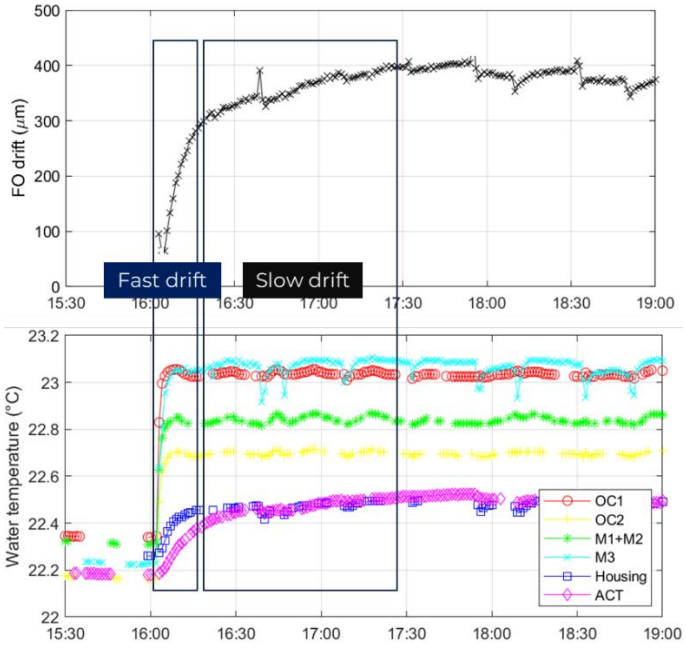

Figure 4.6: Comparison between FO drift and raw temperatures

4.5.2 Contribution of fast and slow expanding structures

With the previous reasoning, the FO drift can be divided into two exponential-like curves that, in different proportions, contribute to the final FO drift. In Figure 4.7, it's presented an example made with an online graphing calculator, *Desmos,* to show how this would work:

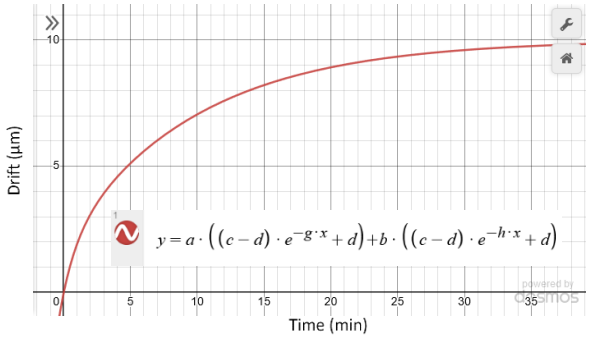

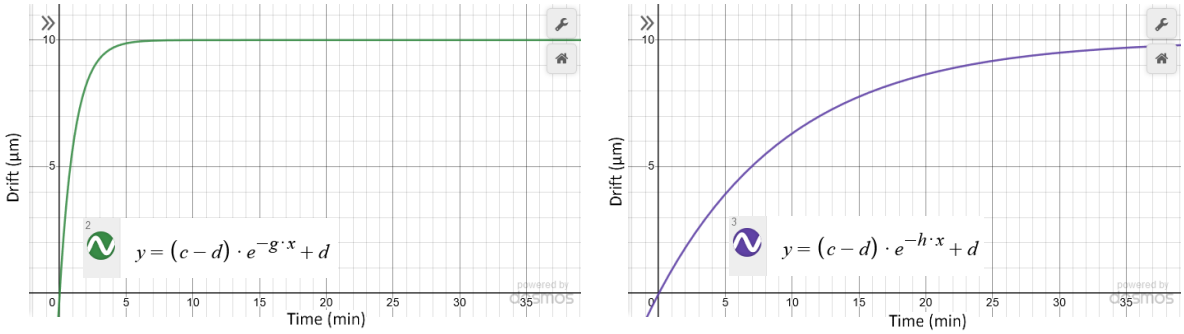

Figure 4.7: Representation of the FO drift signal, as a sum of two curves with *a* and *b* contribution (top), representation of the FO drift signal if *a* contribution was 100%, with a time constant of *1/g* = 1 min (bottom right), representation of the FO drift signal if *b* contribution was 100%, with a time constant of *1/h* = 12.5 min (bottom left).

In Figure 4.7, it is shown a model for the FO drift curve in red, and the fast and slow structures, in green and blue, respectively, that when summed in certain weights, results in the FO drift. The curves are of the type:

$$y = (c - d) \cdot e^{-1/\tau \cdot x} + d \tag{12}$$

Where c is the starting y, d is the final y, and τ, the time constant, which will be different for the fast and slow curves. Since the y axis represents the FO drift (in the Z direction), the equation 12 can be rewritten as equation 13:

$$(Z_i - Z_\infty)e^{-1/\tau \cdot x} + Z_\infty \tag{13}$$

Where both curves share the same Z_i (starting drift) and Z_∞ (ending rift), and their proportion determines their contribution to the total FO drift. However, the time constants differentiate them: the fast drift curve has a lower time constant compared to the slow drift curve. The FO curve model is written as:

$$FO\ drift = A\left((Z_i - Z_\infty)e^{-1/\tau_{fast} \cdot x} + Z_\infty\right) + B\left((Z_i - Z_\infty)e^{-1/\tau_{slow} \cdot x} + Z_\infty\right) \tag{14}$$

Where A and B are the contribution of the fast and slow drift respectively, and are such that:

$$A + B = 1$$

If $A = 0.2$ and $B = 0.8$, the green and blue curve look like those in Figure 4.8, which when summed they follow the FO drift curve.

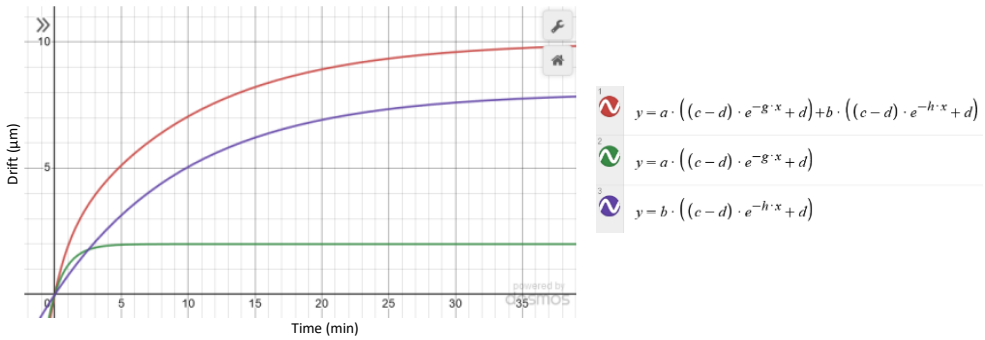

Figure 4.8: Representation of the FO drift curve model (red), as a sum of a fast drift curve with a = 20% of contribution (bottom right), with a time constant of $1/g$ = 1 minute, and a slow drift curve with a b = 80% contribution (bottom left), with a time constant of $1/h$ = 12.5 minutes.

Figure 4.8 helped visualizing the experimental FO drift as a sum of two exponentials with different time constants. The slow drift curve can, however, still be separated in another two curves, with the goal of understanding the difference in contribution between the Housing and ACT.

4.5.3 Contribution of the Housing and Actuation System

The slowest part of the FO drift is coming from a combination of the Housing and ACT thermal expansion, and therefore, the goal is to distinguish the structures that are most impactful for the FO drift. Knowing the fast and slow curves' contribution, this information can be used to separate the slow curve in two, and fit equation 15 in the FO drift curve:

$$FO\ drift = A\left((Z_i - Z_\infty)e^{-1/\tau_{fast}\cdot x} + Z_\infty\right) + B\left(C\left((Z_i - Z_\infty)e^{-1/\tau_{Hous}\cdot x} + Z_\infty\right) + D\left((Z_i - Z_\infty)e^{-1/\tau_{ACT}\cdot x} + Z_\infty\right)\right) \quad (15)$$

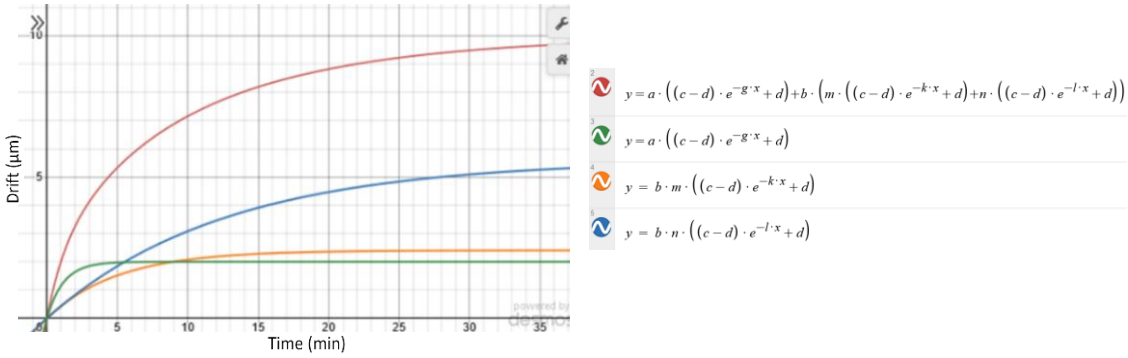

Figure 4.9: Representation of the FO drift curve (red), as a sum of the fast drift curve (green), with a 20% contribution, the Housing curve (yellow) with an 80%*30% (B*C) contribution, and the ACT curve (blue), with an 80%*70% contribution

In Figure 4.9 it is now represented how these curves look like individually, with their own proportion, and their sum, which follows well the FO drift curve (in red). In this specific case the green curve corresponds to the fast drift curve, with $A = 0.2$, the yellow curve corresponds to the contribution of the Housing, with $B = 0.8$ and $C = 0.3$, and the blue curve corresponds to the ACT, with $D = 0.7$.

4.5.4 Results of the contributors to the FO drift

Following the method previously described, the first step is to find the fast and slow curves and their weights (A and B, in equation 14). Equation 14 is fitted to the FO drift data, with Z_i and Z_∞ from the data points and restricting τ_{fast} with the time constants of mirrors and windows, and τ_{slow} with the time constants of the Housing and ACT.

The fittings of the raw temperatures and FO drift, for all machines, can be found in the Appendix A, but it is shown an example of Machine 1, to demonstrate the fitting process. *Curve Fitter* in MATLAB was used to obtain the time constants of W10 and M3, to represent windows and mirrors, and of the Housing and ACT. The process of finding undisturbed data or "perfect" curves can be tedious due to the variations of EUV power, which affects the raw temperature data.

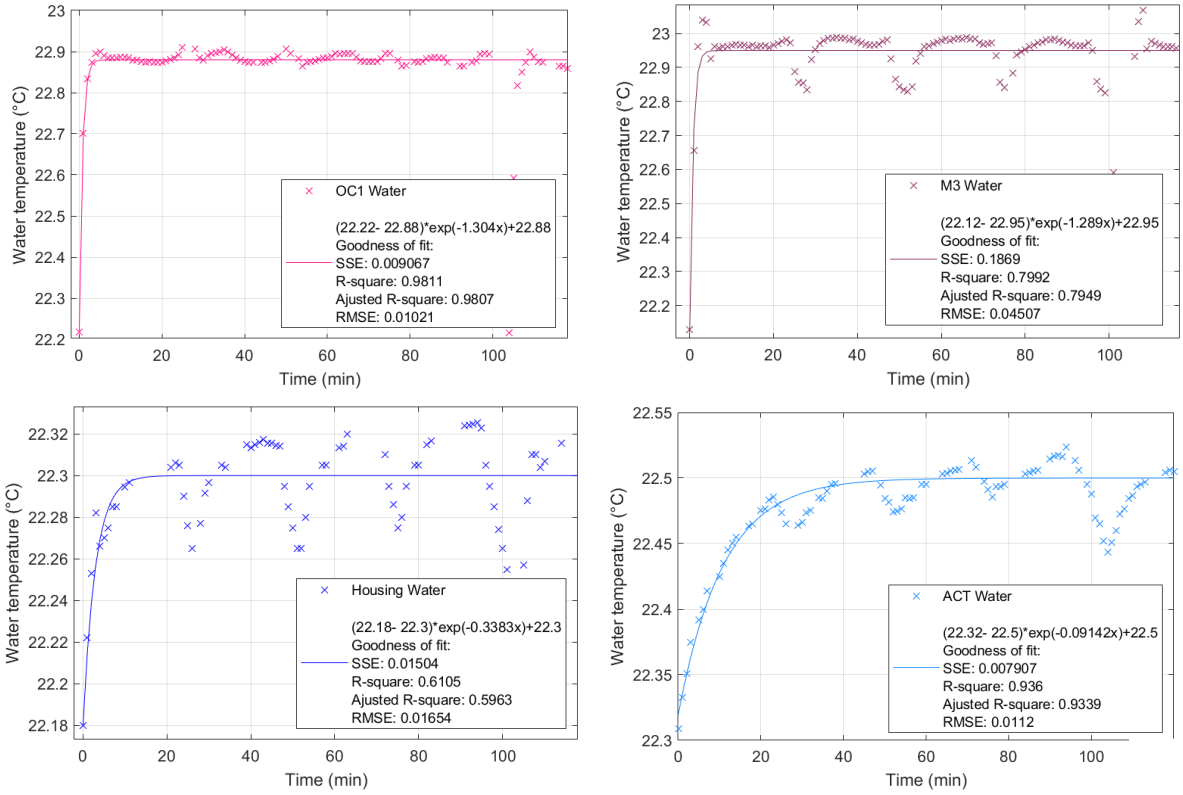

Figure 4.10: Fitting of temperature data of OC1 (top left), M3 (top right), Housing (bottom left) and ACT (bottom right) water temperatures, to find their respective time constants.

Table 4.1 summarizes the time constants obtained by the exponential fitting of W10, M3, Housing and ACT raw temperatures data, of 8 machines. The time constants for W10, M3, are used to restrict the τ_{fast} (τ_{fast} boundary), for the FO drift data fitting, and the time constants for Housing and ACT, are used to restrict the τ_{slow}, (τ_{slow} boundary).

Table 4.1: τ_{fast} and τ_{slow} boundary restrictions

machine	τ fast boundary		τ slow boundary	
	τ OC (min)	τ M (min)	τ Housing (min)	τ ACT (min)
1	0.77	0.78	2.96	10.94
2	0.79	1.61	5.11	16.92
3	0.60	1.35	-	13.64
4	1.11	1.65	3.92	14.88
5	0.73	1.24	11.60	20.60
6	0.65	0.94	3.24	11.03
7	0.75	1.05	3.87	12.21
8	1.39	1.90	4.54	11.76
Avg., μ	0.85	1.31	5.04	14
St. Dev. σ	0.27	0.39	2.98	3.4

It is observed that the Housing is the structure with the highest standard deviation compared to the mean value. In fact, the Housing is the most sensible structure to EUV, which becomes an added difficulty in the fitting process. On top of not having stable EUV signals, the time constants obtained for the Housing are prone to more variation.

Using machine 1 as an example and fitting the FO drift data points in the equation 14, the approximate values of fast drift contribution and slow drift contribution are found, as shown in Figure 4.11.

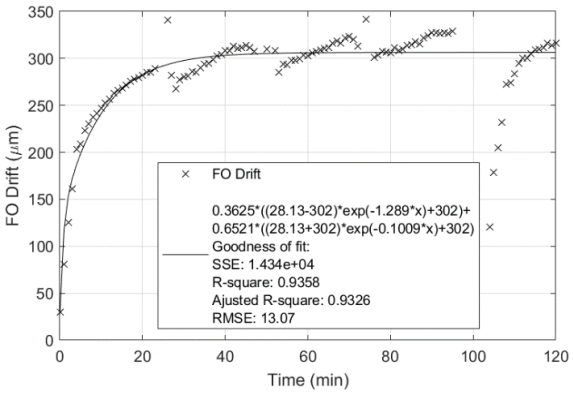

Figure 4.11: FO drift of machine 1 and respective fitting curve with a 36.25% fast drift contribution and a 65.21% slow drift contribution.

Repeating the same process for the 8 machines in study, Table 4.2 reveals a contribution of, on average, 30% for the fast drift, with a standard deviation of 11%, and a contribution of, on average, 70% for the slow drift, with a standard deviation of 11%. Variations of EUV are the main source of errors for these fittings, which is why the fast and slow drift contributions can vary from machine to machine.

Table 4.2: Obtained τ_{fast} and τ_{slow} values and contributions of the fast and slow drift.

machine	τ fast (min)	% fast	τ slow (min)	% slow
1	0.78	36.3%	9.91	65.2%
2	1.45	21.8%	14.29	79.9%
3	0.88	25.1%	11.11	75.6%
4	1.65	27.0%	13.06	73.6%
5	1.24	34.3%	17.65	66.3%
6	0.94	39.2%	8.12	61.1%
7	1.05	12.5%	9.09	87.8%
8	1.25	48.2%	10.71	51.4%
Avg., μ	1.1	30%	11.7	70%
St. Dev., σ	0.30	11%	3.12	11%

The next step utilizes the obtained fast and slow drift contributions to find the contributions of the Housing and ACT thermal expansion to the FO drift (C and D, in equation 15), using the previously obtained τ_{Hous}, τ_{ACT}.

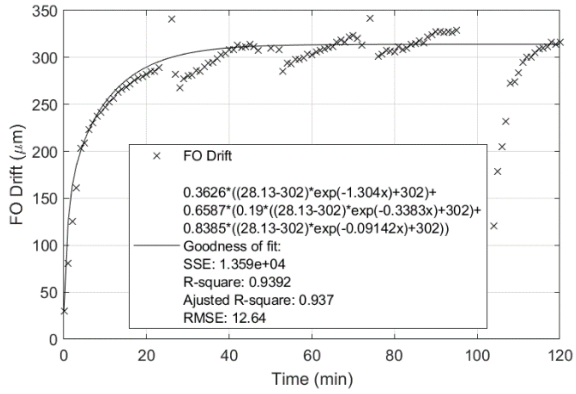

Figure 4.12: FO drift of machine 1 and respective fitting curve with a 36% fast drift contribution, 13% for the housing expansion contribution, and 56% for the ACT expansion contribution.

In Table 4.3, there can be found the results for this fitting, suggesting that the ACT's thermal expansion is responsible for, on average, 56% of the FO drift, with a standard deviation of 16%, stated in Table 4.4. In other words, the results suggest that the ACT's thermal expansion is contribution for most of the actuator's correction of the FO drift.

Table 4.3: Obtained contributions of the Housing and ACT for the slow drift.

machine	% Housing	% ACT
1	19.0%	83.9%
2	12.1%	87.4%
3	12.3%	86.9%
4	15.3%	85.8%
5	28.0%	73.5%
6	39.2%	68.6%
7	34.7%	68.1%
8	22.4%	82.7%
Avg., μ	23%	80%
St. Dev., σ	10%	8%

Table 4.4: Average of the overall contributions of every expansion for the FO drift.

	Average contribution, μ	Standard Deviation, σ
Optics (fast drift)	30%	11%
Housing	14%	15%
ACT	56%	16%

The values obtained from Table 4.2 and Table 4.4 are combined to form the final diagram in Figure 4.13, where all the contributions can be better compared and visualized. In this diagram, it is clearly seen the ACT's impact in comparison to the remaining structures.

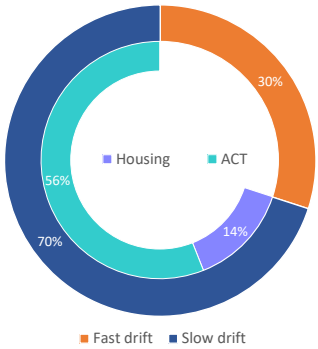

Figure 4.13: Diagram representing each contribution for the FO drift, which impacts the actuation range

However, some inaccuracies may emerge from this method, which is the case of using time constants that are not exactly the time constants of the structures' cooling water, because there is never a case of non-varying EUV power. Using these time constants to fit other data points that are also not perfect curves result in an accumulating of errors that are seen in the SSE or RMSE values.

Regardless, between themselves, the values of the Housing and ACT contributions for the slow drift are consistent and reveal a first step to find the root cause for the actuator's range. More research shall be done to confirm this result, given the fact that this could not be the perfect approach. FEM simulations are necessary to corroborate the contributions of each structure obtained to the actuation range.

5

CONCLUSION AND FUTURE WORK

5.1 Conclusions

The trend to increase EUV power in lithography machines implied a profound study of the impact back-reflected heat loads have on the thermo-mechanics of the components in the Focusing Optics. This meant quantifying back-reflections in the FO and correlating with the actuation range, which corrects for thermal expansions. In this regard, a MATLAB script that processes raw machine data, (return water temperatures and Actuator displacement), to calculate the heat loads towards FU structures and actuation range, was successfully created. Its main features are:

- Obtains only stable water temperature values from raw water temperature data sets, meaning that it removes nonstable data that is not useful for statistics.
- Obtains cold water temperatures, needed to calculate minutely thermal parameters necessary for this study: ΔT, absorbed power and absorption response, instead of the available hourly KPIs.
- Calculates the magnitude of the FO drift, that is corrected by the ACT.

With this data, it was possible to plot a population of multiple machines for the ΔT, absorbed power, absorption response, for a population of multiple machines. It was concluded that the M3, the Housing and the ACT are the most impacted by back-reflected heat loads. From the statistical analysis of data, it was mainly concluded that:

- Comparison shows that the M3 is impacted by back-reflected heat loads. The M1 and M2 don't present a significant impact from back-reflected heat loads.
- The Housing and ACT are also impacted by back-reflected heat loads, due the fact that they do not reflect the forward beam but have a non-zero absorption response.
- Absorbed power in M3, Housing and ACT correlate with the CO_2 drive laser power, however it was not possible to find a correlation between absorbed back-reflected power by M3 (absorbed power minus absorbed power from forward beam) due to errors calculating absorbed power from forward beam (these errors interfere with the already low correlation with CO_2 laser power, due to the high reflectivity of M3).

It was concluded that the FO drift has a strong correlation with back-reflected power (any power absorbed by Housing+ACT water is, in principle, from back-reflections). The Actuator-Z range also showed a correlation with back-reflected power which was confirmed with the Machine A (which is a system with higher back-reflected heat loads).

It was performed a study to find the FO structure that contributes the most for the FO drift, through each structure's time constant and comparison with FO drift signal:

- It was found that the FO drift is composed of at least a sum of a curve for the fast drift (optical components), with a 30% contribution, and a curve for slow drift (Housing and ACT), with a 70% contribution.
- The Housing has a contribution of 23% for the slow drift, while the ACT has a contribution of 80%. This suggested that the ACT's thermal expansion has the biggest impact in the overall FO drift, with a contribution of, on average 56%. With this result, the ACT was found to be the possible root cause for the actuation range that corrects the FO drift (while the results show apparent evidence, this needs to be confirmed by FEM simulations).
- The method used is still prone to inaccuracies, that are visible in the SSE or RMSE values from the FO drift fitting. The variations in EUV result in fitting errors that accumulate with the use of results from successive fittings.

Despite the limitations, this investigation was a step forward in the research to find the main root cause for the actuator's range, as well as a successful contribution for providing statistical thermal and actuation data, for the FO, for a population of multiple machines and a MATLAB script capable of extending this research to either more water-cooled components or different machines. The manufacturer is now aware of the influence and possible outcomes that may emerge from increasing back-reflections, in the thermo-mechanics of the FO.

5.2 Future work

- The created MATLAB script can be extended to the BTS and other modules and provide statistical thermal data and a complete detailed thermal description of all water-cooled components.
- The method used to find the main contributor to the FO drift allowed cumulative errors that began in fittings to find the time constants of W10, M3, Housing and ACT. The temperature curves can be extremely sensitive to EUV variations, which results in some errors. This is also the case for the FO drift curve fitting. For better results, tests with non-varying EUV, for at least 120 minutes after switching ON the drive laser, shall be generated, which has not yet been found in any machine, with decent search.
- For a better understanding of the main contribution for the FO drift, a FEM simulation shall be performed to confirm the results of this investigation and provide more in-depth knowledge of the interaction between the FO drift and ACT correction.
- Drive laser astigmatism (ast) is thought to likely increase with power, therefore a statistical study with a population of multiple machines for astigmatism and a subsequent correlation study between atigmatism and EUV/CO_2 drive laser power shall be introduced, to investigate the consequences for increasing power and ways of compensation. The MATLAB code is ready to be adapted for this parameter.

6

REFERENCES

[1] Q. Wu, Y. Li, and Y. Zhao, "The Evolution of Photolithography Technology, Process Standards, and Future Outlook," *2020 IEEE 15th International Conference on Solid-State and Integrated Circuit Technology, ICSICT 2020 - Proceedings*, Nov. 2020, doi: 10.1109/ICSICT49897.2020.9278164.

[2] I. Fomenkov *et al.*, "Light sources for high-volume manufacturing EUV lithography: Technology, performance, and power scaling," *Advanced Optical Technologies*, vol. 6, no. 3–4, pp. 173–186, Jun. 2017, doi: 10.1515/AOT-2017-0029/MACHINEREADABLECITATION/RIS.

[3] T. Tomie, "Tin laser-produced plasma as the light source for extreme ultraviolet lithography high-volume manufacturing: history, ideal plasma, present status, and prospects," *Journal of Micro/Nanolithography, MEMS, and MOEMS*, vol. 11, no. 2, pp. 021109–1, May 2012, doi: 10.1117/1.JMM.11.2.021109.

[4] P. Giesen and E. Folgering, "Design guidelines for thermal stability in optomechanical instruments," *Optomechanics 2003*, p. 126, Oct. 2003, doi: 10.1117/12.510285.

[5] Q. Wu, Y. Li, and Y. Zhao, "The Evolution of Photolithography Technology, Process Standards, and Future Outlook," *2020 IEEE 15th International Conference on Solid-State and Integrated Circuit Technology, ICSICT 2020 - Proceedings*, Nov. 2020, doi: 10.1109/ICSICT49897.2020.9278164.

[6] "'We underestimated the demand for DUV' – Bits&Chips." Accessed: Sep. 27, 2023. [Online]. Available: https://bits-chips.nl/artikel/we-underestimated-the-demand-for-duv/

[7] V. Bakshi, H. Mizoguchi, T. Liang, A. Grenville, J. Benschop, and " Euv, "Special Section Guest Editorial: EUV Lithography for the 3-nm Node and Beyond," *https://doi.org/10.1117/1.JMM.16.4.041001*, vol. 16, no. 4, Dec. 2017, doi: 10.1117/1.JMM.16.4.041001.

[8] M. A. van de Kerkhof, J. P. H. Benschop, and V. Y. Banine, "Lithography for now and the future," *Solid State Electron*, vol. 155, pp. 20–26, May 2019, doi: 10.1016/J.SSE.2019.03.006.

[9] Institute of Electrical and Electronics Engineers. and Optical Society of America., "Excimer laser lithography," *Conference on Lasers and Electro-Optics (1987), paper THN1*, p. THN1, Apr. 1987, Accessed: Sep. 27, 2023. [Online]. Available: https://opg.optica.org/abstract.cfm?uri=CLEO-1987-THN1

[10] H. Jinbo and Y. Yamashita, "0.2 μm or less i-line lithography by phase-shifting-mask technology," *Tech Dig Int Electron Devices Meet*, pp. 825–828, Dec. 1990, doi: 10.1109/IEDM.1990.237035.

[11] R. W. McCleary *et al.*, "Performance Of A KrF Excimer Laser Stepper," *https://doi.org/10.1117/12.968437*, vol. 2, pp. 396–399, Jan. 1988, doi: 10.1117/12.968437.

[12] J. Song, C. H. Kim, and G. W. Lee, "A Study on the Resolution and Depth of Focus of ArF Immersion Photolithography," *Micromachines 2022, Vol. 13, Page 1971*, vol. 13, no. 11, p. 1971, Nov. 2022, doi: 10.3390/MI13111971.

[13] A. C. Tung and H. Wan, "Organisational Investment: The Case of ASML—Can the Product Make the Producer?," *https://doi.org/10.1177/00157325221127606*, vol. 58, no. 1, pp. 176–191, Oct. 2022, doi: 10.1177/00157325221127606.

[14] Y. Nishimura *et al.*, "Key technology development progress of the high power LPP-EUV light source," *https://doi.org/10.1117/12.2612778*, vol. 12051, pp. 241–255, May 2022, doi: 10.1117/12.2612778.

[15] H. M. Saavedra *et al.*, "Microdroplet-tin plasma sources of EUV radiation driven by solid-state-lasers (Topical Review)," *Journal of Optics*, vol. 24, no. 5, p. 054014, Apr. 2022, doi: 10.1088/2040-8986/AC5A7E.

[16] I. Fomenkov, "EUV Source for High Volume Manufacturing: Performance at 250 W and Key Technologies for Power Scaling," 2017.

[17] H. Mizoguchi, H. Nakarai, Y. Usami, K. Kakizaki, J. Fujimoto, and T. Saitou, "High-power LPP-EUV source for semiconductor HVM: lithography and other applications," *https://doi.org/10.1117/12.2657787*, vol. 12292, pp. 255–260, Dec. 2022, doi: 10.1117/12.2657787.

[18] D.-K. Yang *et al.*, "The development of laser-produced plasma EUV light source," *Chip*, vol. 1, no. 3, p. 100019, Sep. 2022, doi: 10.1016/J.CHIP.2022.100019.

[19] A. A. Schafgans *et al.*, "Performance optimization of MOPA pre-pulse LPP light source," *https://doi.org/10.1117/12.2087421*, vol. 9422, pp. 56–66, Mar. 2015, doi: 10.1117/12.2087421.

[20] I. Fomenkov *et al.*, "Light sources for high-volume manufacturing EUV lithography: Technology, performance, and power scaling," *Advanced Optical Technologies*, vol. 6, no. 3–4, pp. 173–186, Jun. 2017, doi: 10.1515/AOT-2017-0029/MACHINEREADABLECITATION/RIS.

[21] M. A. van de Kerkhof *et al.*, "High-power EUV lithography: spectral purity and imaging performance," *https://doi.org/10.1117/1.JMM.19.3.033801*, vol. 19, no. 3, p. 033801, Sep. 2020, doi: 10.1117/1.JMM.19.3.033801.

[22] K. D. Closser, D. F. Ogletree, P. Naulleau, and D. Prendergast, "The importance of inner-shell electronic structure for enhancing the EUV absorption of photoresist materials," *Journal of Chemical Physics*, vol. 146, no. 16, Apr. 2017, doi: 10.1063/1.4981815/13577582/164106_1_ACCEPTED_MANUSCRIPT.PDF.

[23] A. Dolgov *et al.*, "Extreme ultraviolet (EUV) source and ultra-high vacuum chamber for studying EUV-induced processes," *Plasma Sources Sci Technol*, vol. 24, no. 3, p. 035003, Apr. 2015, doi: 10.1088/0963-0252/24/3/035003.

[24] E. Louis *et al.*, "Progress in Mo/Si multilayer coating technology for EUVL optics," *https://doi.org/10.1117/12.390077*, vol. 3997, pp. 406–411, Jul. 2000, doi: 10.1117/12.390077.

[25] J. Bosgra *et al.*, "Structural properties of subnanometer thick Y layers in extreme ultraviolet multilayer mirrors," *Applied Optics, Vol. 51, Issue 36, pp. 8541-8548*, vol. 51, no. 36, pp. 8541–8548, Dec. 2012, doi: 10.1364/AO.51.008541.

[26] "EUV lithography systems – Products | ASML." Accessed: Sep. 27, 2023. [Online]. Available: https://www.asml.com/en/products/euv-lithography-systems

[27] D. C. Brandt *et al.*, "LPP EUV source development for HVM," *https://doi.org/10.1117/12.713279*, vol. 6517, pp. 230–239, Mar. 2007, doi: 10.1117/12.713279.

[28] A. Bajard, O. Aubreton, G. Eren, P. Sallamand, and F. Truchetet, "3D digitization of metallic specular surfaces using scanning from heating approach," *https://doi.org/10.1117/12.872467*, vol. 4, pp. 373–379, Jan. 2011, doi: 10.1117/12.872467.

[29] F. P. Incropera, D. P. DeWitt, T. L. Bergman, and A. S. Lavine, *Fundamentals of Heat and Mass Transfer. Sixth Edition*. 2011.

[30] M. F. Ashby, "Material and Process Seleciton Charts for Engineering Design," *The CES EduPack Resource Booklet 2*, p. 42, 2010.

[31] Bela G. Liptak, *Instrument Engineers' Handbook, Fourth Edition, Volume One: Process Measurement and Analysis*, vol. 1. CRC Press, 2003.

[32] K. Smith and P. Holroyd, *Engineering Principles for Electrical Technicians: The Commonwealth and International Library: Electrical Engineering Division*, 1st ed., vol. 1. Pergamon, 2013.

[33] The Engineering ToolBox, "Solids, Liquids and Gases - Thermal Conductivities." Accessed: Sep. 27, 2023. [Online]. Available: https://www.engineeringtoolbox.com/thermal-conductivity-d_429.html

[34] The Engineering ToolBox, "Metals - Specific Heats." Accessed: Sep. 27, 2023. [Online]. Available: https://www.engineeringtoolbox.com/specific-heat-metals-d_152.html

[35] The Engineering ToolBox, "Piping Materials - Temperature Expansion Coefficients." Accessed: Sep. 27, 2023. [Online]. Available: https://www.engineeringtoolbox.com/pipes-temperature-expansion-coefficients-d_48.html

[36] F. Incropera, D. DeWitt, T. Bergman, and A. Lavine, *Fundamentals of Heat and Mass Transfer. Sixth Edition*. 2011.

[37] J. M. Lourenço, "The NOVAthesis LATEX Template User's Manual. NOVA University Lisbon." [Online]. Available: https://github.com/joaomlourenco/novathesis_word/raw/master/novathesis_word-FINAL-EN.pdf

A

APPENDIX

A.1 Curve fitting characterization for machines 2-8

Machine 2

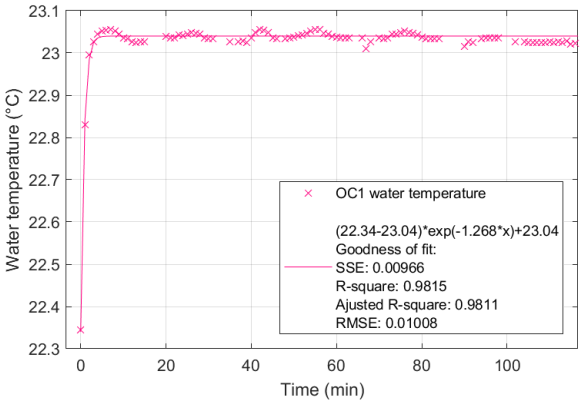

Figure 6.1: Fitting of water temperature data of OC1, and respective fitting parameters, for machine 2

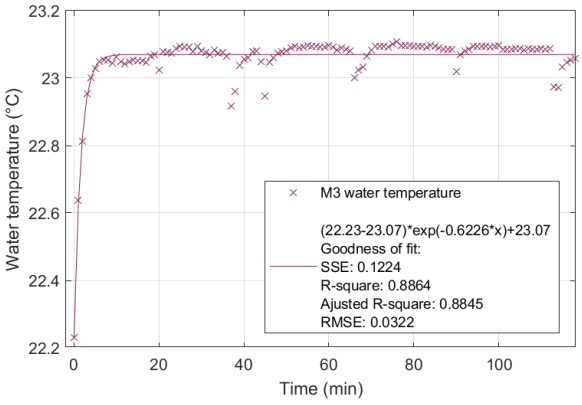

Figure 6.2: Fitting of water temperature data of M3, and respective fitting parameters, for machine 2

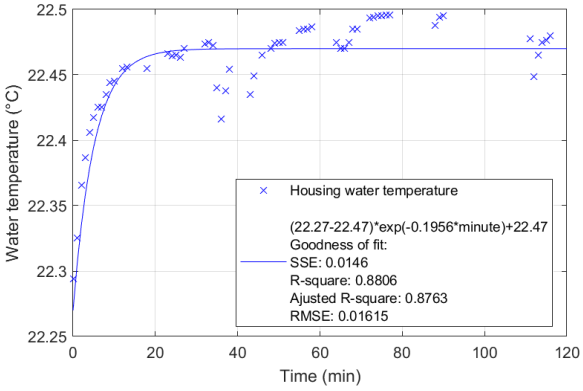

Figure 6.3: Fitting of water temperature data of Housing, and respective fitting parameters, for machine 2

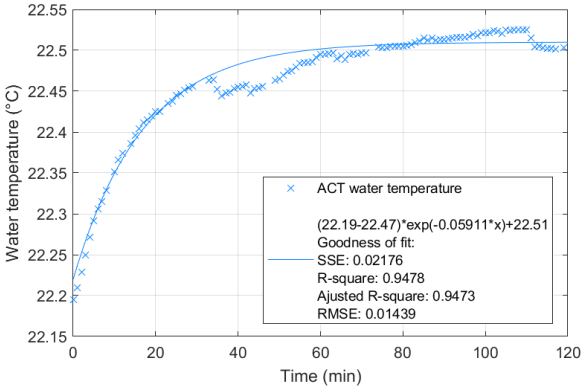

Figure 6.4: Fitting of water temperature data of ACT, and respective fitting parameters, for machine 2

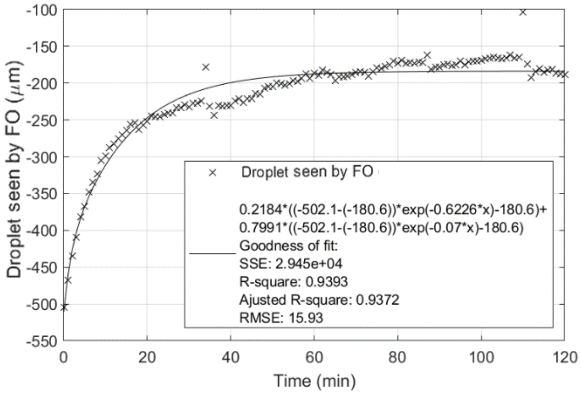

Figure 6.5: Fitting of the FO drift to get the comtributions of fast and slow drift for the machine 2

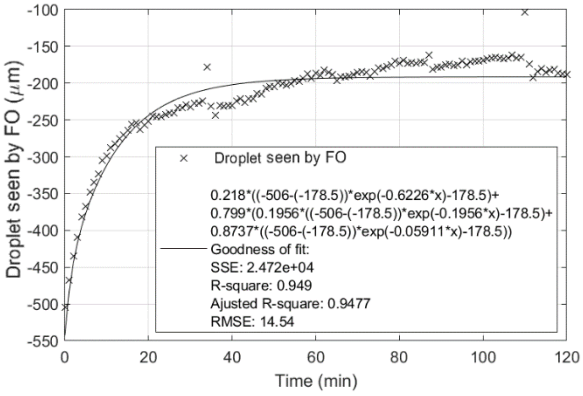

Figure 6.6: Fitting of the FO drift to obtain the contributions of Housing and ACT expansion, for machine 2

Machine 3

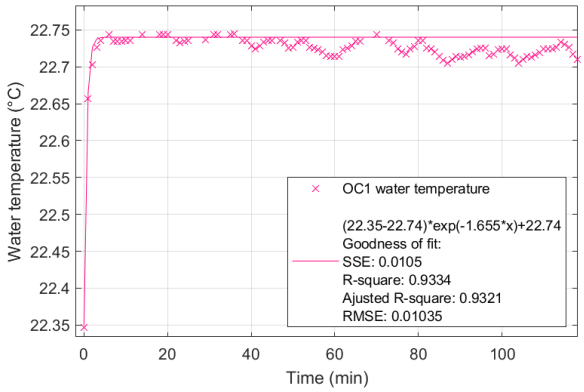

Figure 6.7: Fitting of water temperature data of OC1, and respective fitting parameters, for machine 3

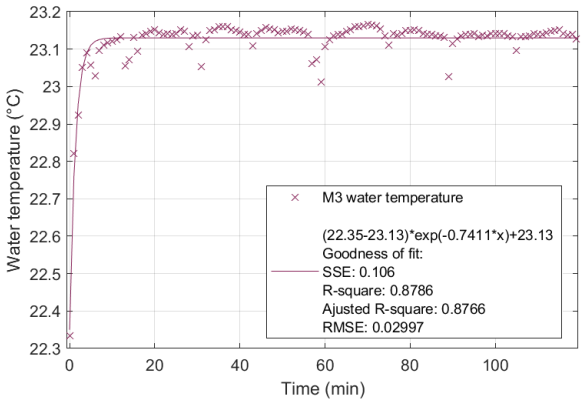

Figure 6.8: Fitting of water temperature data of M3, and respective fitting parameters, for machine 3

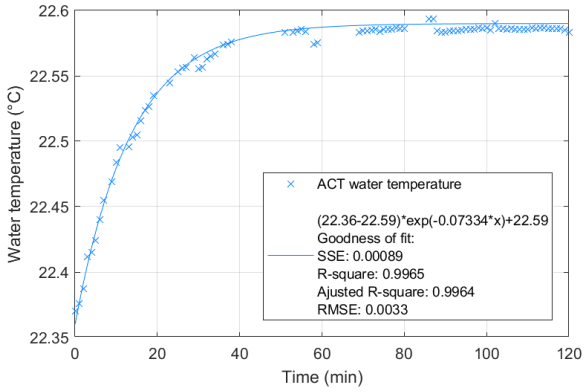

Figure 6.9: Fitting of water temperature data of ACT, and respective fitting parameters, for machine 3

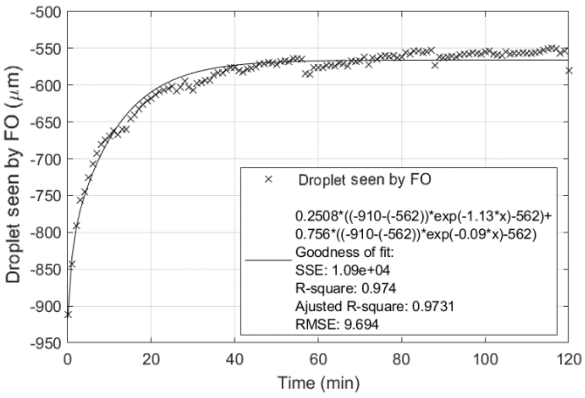

Figure 6.10: Fitting of the FO drift to get the comtributions of fast and slow drift for the machine 3

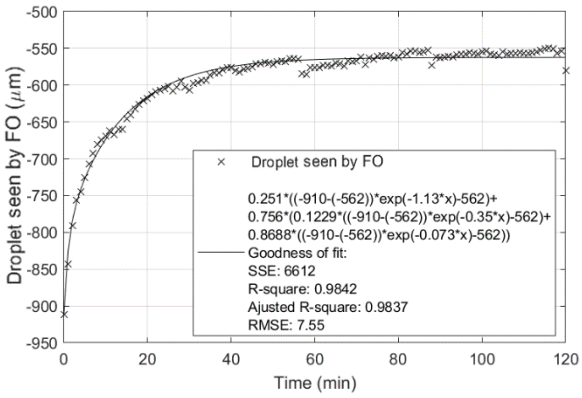

Figure 6.11: Fitting of the FO drift to obtain the contributions of Housing and ACT expansion, for machine 3

Machine 4

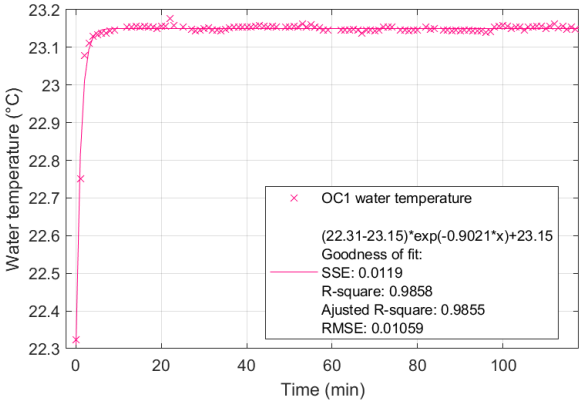

Figure 6.12: Fitting of water temperature data of OC1, and respective fitting parameters, for machine 4

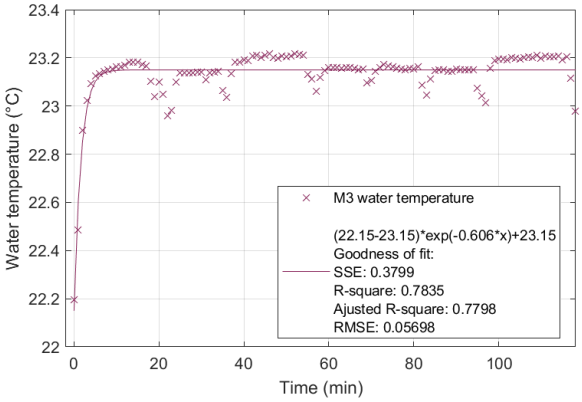

Figure 6.13: Fitting of water temperature data of M3, and respective fitting parameters, for machine 4

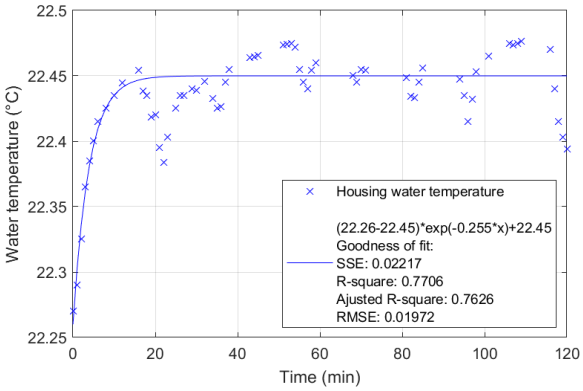

Figure 6.14: Fitting of water temperature data of Housing, and respective fitting parameters, for machine 4

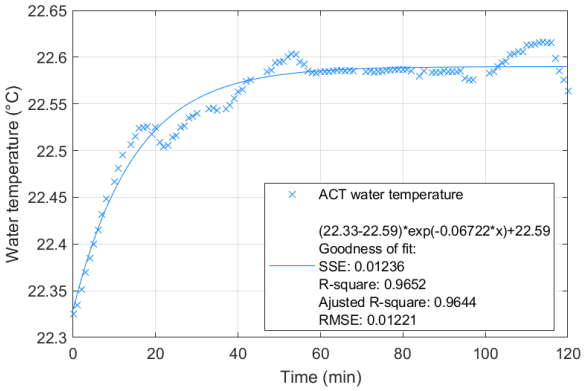

Figure 6.15: Fitting of water temperature data of ACT, and respective fitting parameters, for machine 4

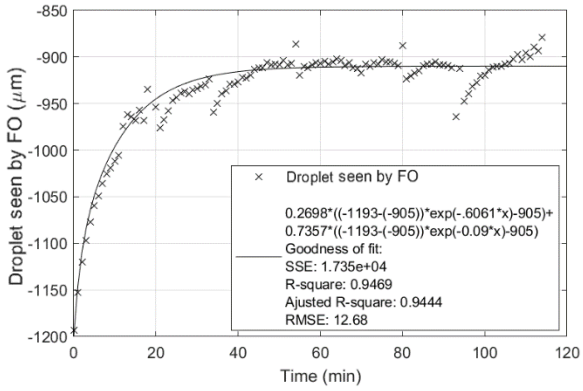

Figure 6.16: Fitting of the FO drift to get the comtributions of fast and slow drift for the machine 4

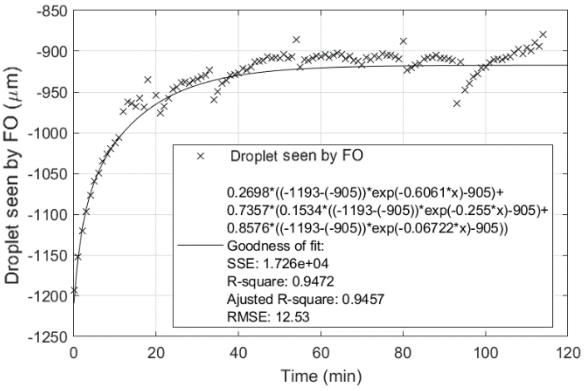

Figure 6.17: Fitting of the FO drift to obtain the contributions of Housing and ACT expansion, for machine 4

Machine 5

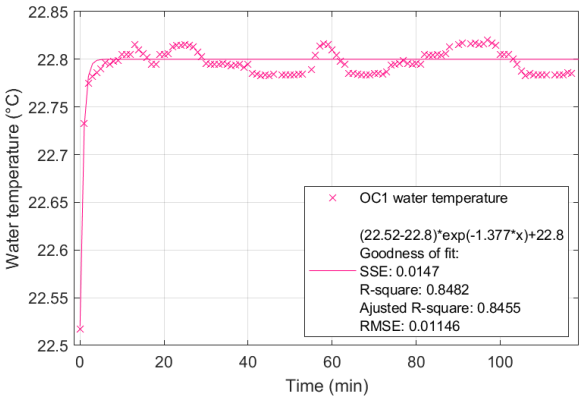

Figure 6.18: Fitting of water temperature data of OC1, and respective fitting parameters, for machine 5

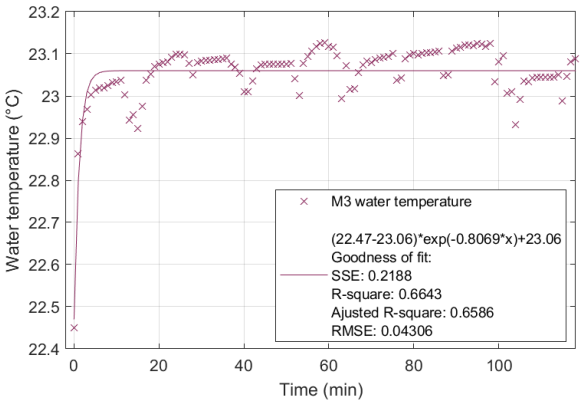

Figure 6.19: Fitting of water temperature data of M3, and respective fitting parameters, for machine 5

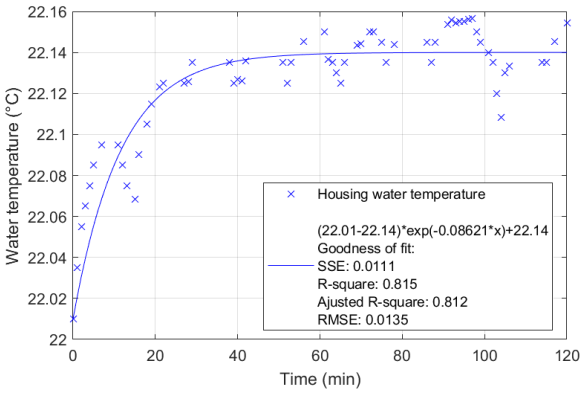

Figure 6.20: Fitting of water temperature data of Housing, and respective fitting parameters, for machine 5

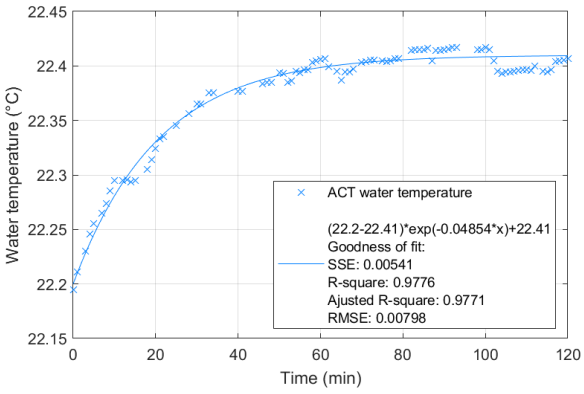

Figure 6.21: Fitting of water temperature data of ACT, and respective fitting parameters, for machine 5

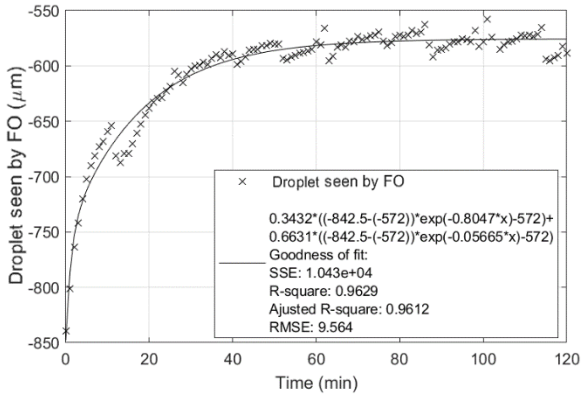

Figure 6.22: Fitting of the FO drift to get the comtributions of fast and slow drift for the machine 5

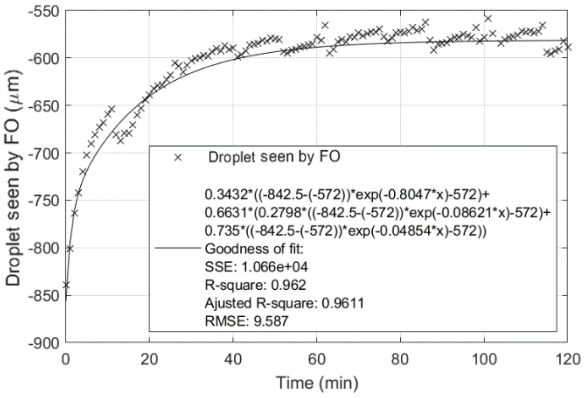

Figure 6.23: Fitting of the FO drift to obtain the contributions of Housing and ACT expansion, for machine 5

Machine 6

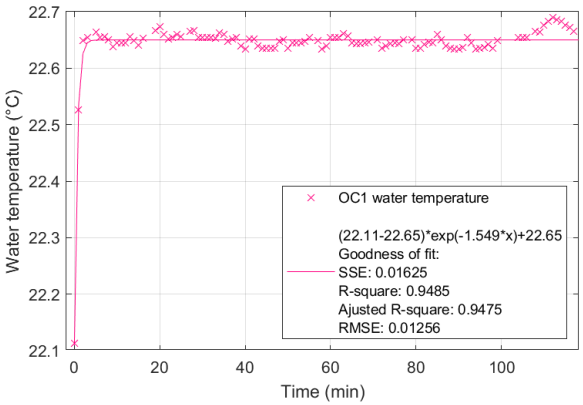

Figure 6.24: Fitting of water temperature data of OC1, and respective fitting parameters, for machine 6

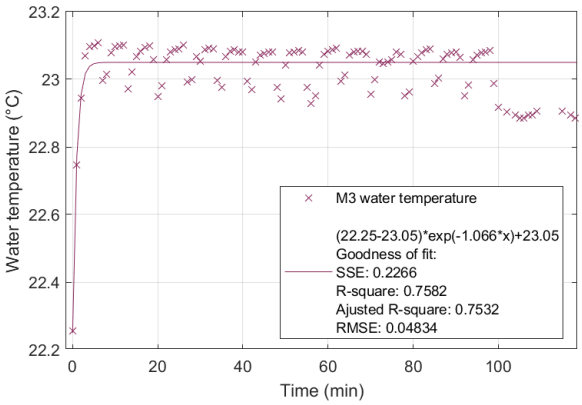

Figure 6.25: Fitting of water temperature data of M3, and respective fitting parameters, for machine 6

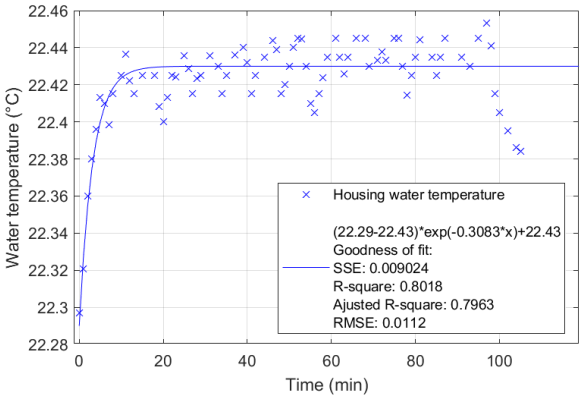

Figure 6.26: Fitting of water temperature data of Housing, and respective fitting parameters, for machine 6

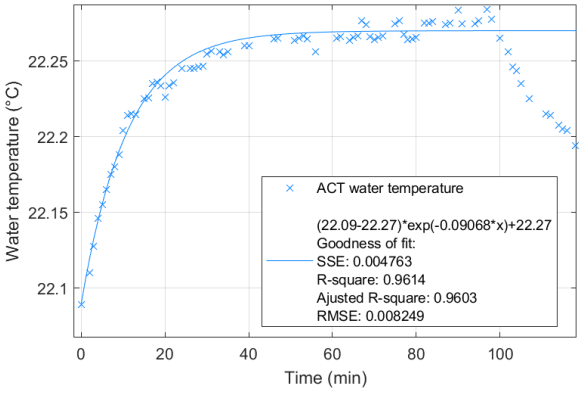

Figure 6.27: Fitting of water temperature data of ACT, and respective fitting parameters, for machine 6

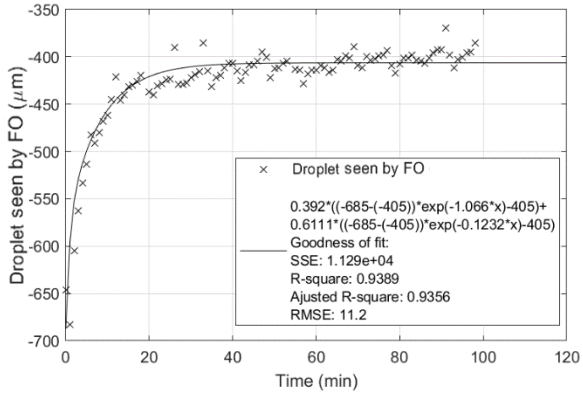

Figure 6.28: Fitting of the FO drift to get the comtributions of fast and slow drift for the machine 6

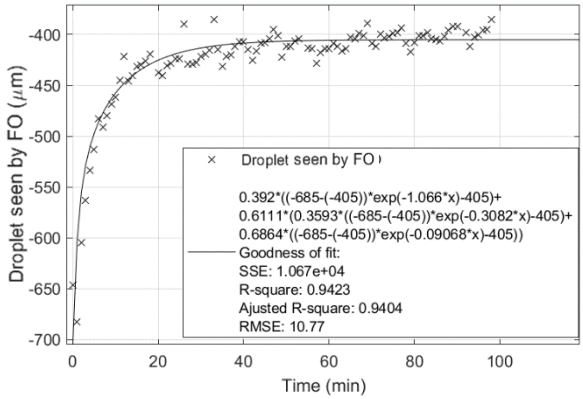

Figure 6.29: Fitting of the FO drift to obtain the contributions of Housing and ACT expansion, for machine 6

Machine 7

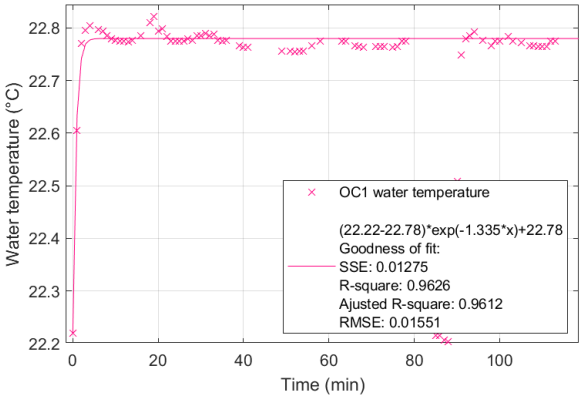

Figure 6.30: Fitting of water temperature data of OC1, and respective fitting parameters, for machine 7

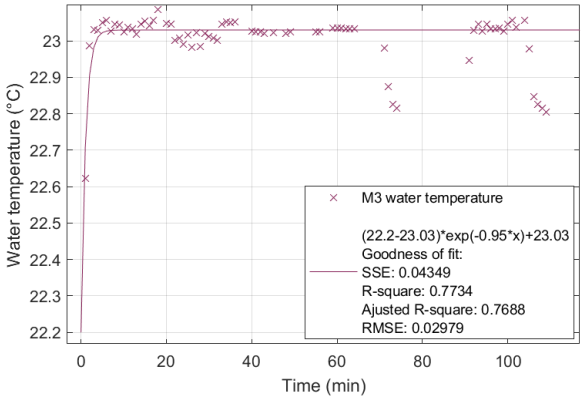

Figure 6.31: Fitting of water temperature data of M3, and respective fitting parameters, for machine 7

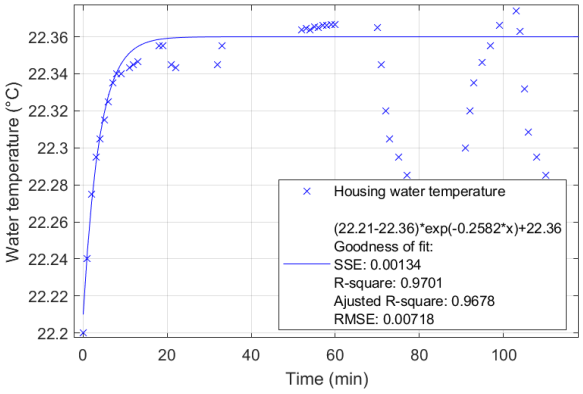

Figure 6.32: Fitting of water temperature data of Housing, and respective fitting parameters, for machine 7

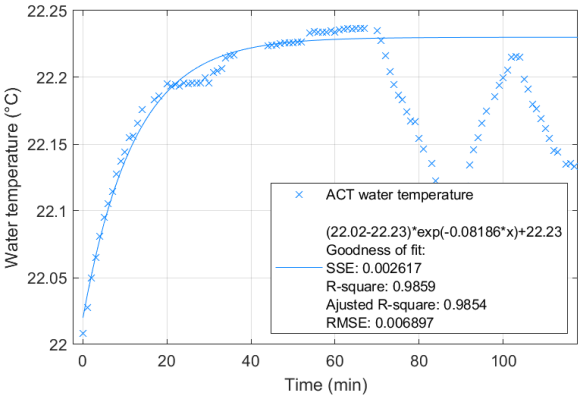

Figure 6.33: Fitting of water temperature data of ACT, and respective fitting parameters, for machine 7

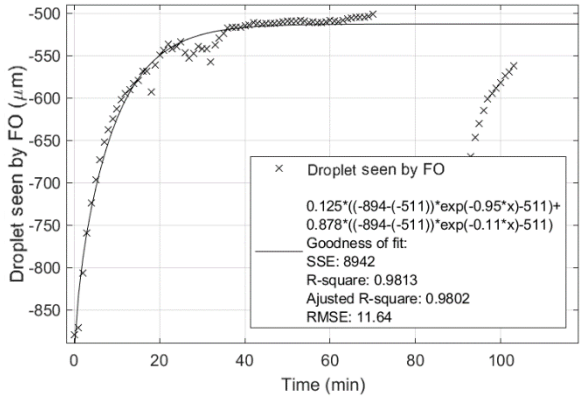

Figure 6.34: Fitting of the FO drift to get the comtributions of fast and slow drift for the machine 7

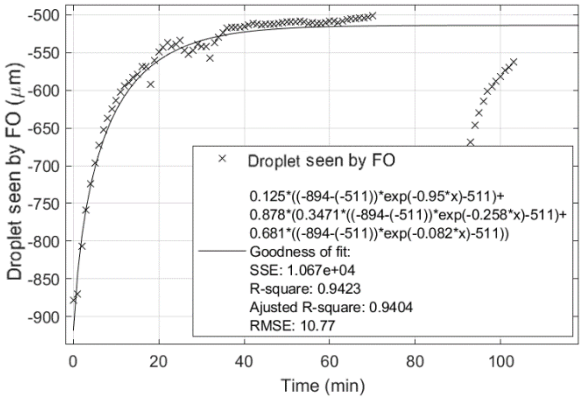

Figure 6.35: Fitting of the FO drift to obtain the contributions of Housing and ACT expansion, for machine 7

Machine 8

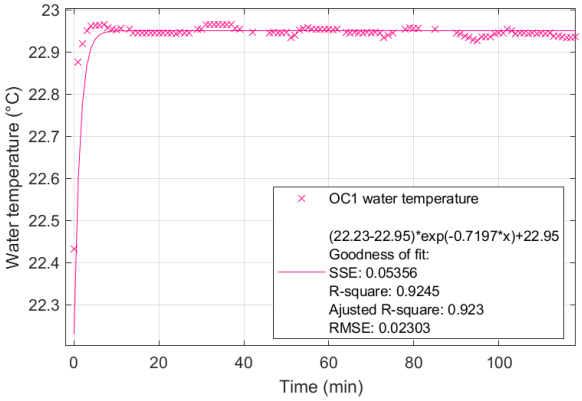

Figure 6.36: Fitting of water temperature data of OC1, and respective fitting parameters, for machine 8

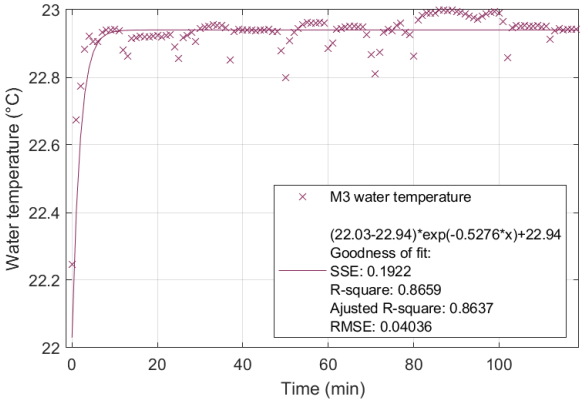

Figure 6.37: Fitting of water temperature data of M3, and respective fitting parameters, for machine 8

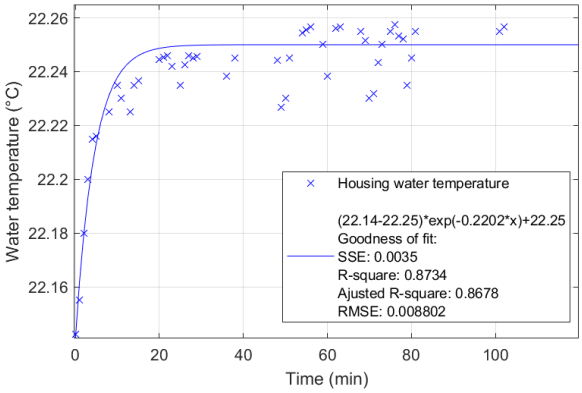

Figure 6.38: Fitting of water temperature data of Housing, and respective fitting parameters, for machine 8

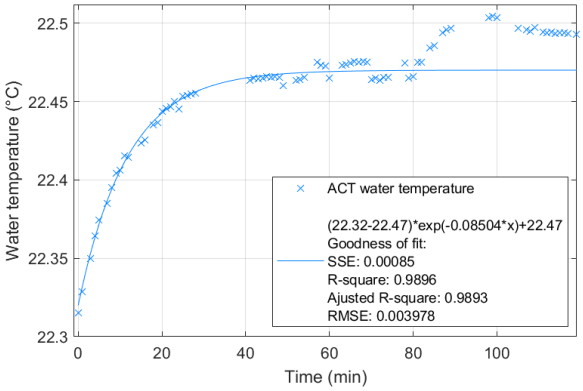

Figure 6.39: Fitting of water temperature data of ACT, and respective fitting parameters, for machine 8

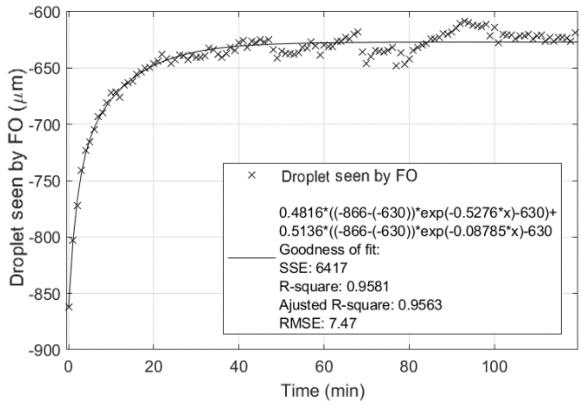

Figure 6.40: Fitting of the FO drift to get the comtributions of fast and slow drift for the machine 8

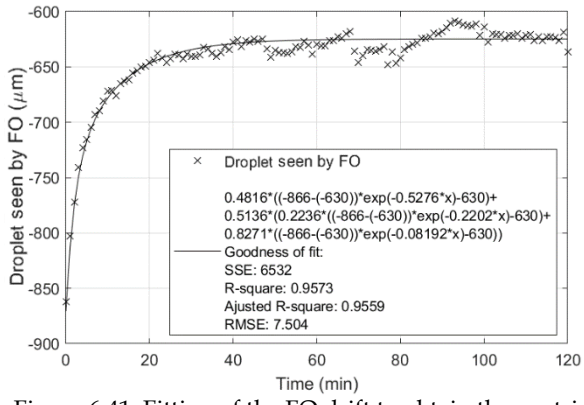

Figure 6.41: Fitting of the FO drift to obtain the contributions of Housing and ACT expansion, for machine 8